CFD predictions of drag force for a Slocum ocean glider

Seo, Dong Cheol; Williams, Christopher D.

Publisher's version / Version de l'éditeur:
https://doi.org/10.4224/17210700
Technical Report (National Research Council Canada); no. TR-2010-07, 2010-04

DOCUMENTATION PAGE

REPORT NUMBER	NRC REPORT NUMBER	DATE
TR-2010-07		April 2010
REPORT SECURITY CLASSIFICATION		**DISTRIBUTION**
Unclassified		Unlimited

TITLE

CFD Predictions of Drag Force for a Slocum Ocean Glider

AUTHOR (S)

Dong Cheol Seo and Christopher D. Williams

CORPORATE AUTHOR (S)/PERFORMING AGENCY (S)

Institute for Ocean Technology, National Research Council, St. John's, NL

PUBLICATION

SPONSORING AGENCY(S)

IOT PROJECT NUMBER	NRC FILE NUMBER
42-2407-16	

KEY WORDS	PAGES	FIGS.	TABLES
Computational Fluid Dynamics, CFD, Ocean Glider, Turbulence models, ANSYS-CFX, ANSYS-FLUENT	v, 44	43	8

SUMMARY

Preceding the installation of a hydro-acoustic monitoring system on an ocean glider, CFD (Computational Fluid Dynamics) tools can be used to assess the impact on the hydrodynamic properties of the glider when the hull is modified because of adding new sensors. In this study, two simple questions are examined. The first one is which CFD code can predict more accurately the drag force of the ocean glider. The second is which turbulence model is appropriate for estimating the drag force at the glide speed of the ocean glider. The CFD results are compared with the results from the drag measurements and self-propulsion experiments which were conducted at the Marine Institute's Flume Tank with a Slocum glider in October and November 2009. Starting from the comparison with the experiments, the comparative study is performed with the help of graphical results such as velocity profiles, pressure contours and wall shear stress distributions. Finally, an analysis is presented for why there are differences between the experimental and predicted values of the drag force according to the two CFD codes and turbulence models which were used.

ADDRESS National Research Council
Institute for Ocean Technology
Arctic Avenue, P. O. Box 12093
St. John's, NL A1B 3T5
Tel.: (709) 772-5185, Fax: (709) 772-2462

National Research Council Canada
Institute for Ocean Technology

Conseil national de recherches Canada
Institut des technologies océaniques

CFD PREDICTIONS OF DRAG FORCE FOR A SLOCUM OCEAN GLIDER

TR-2010-07

Dong Cheol Seo and Christopher D. Williams

April 2010

TABLE OF CONTENTS

LIST OF FIGURES

LIST OF TABLES

1 OVERVIEW

A preliminary series of CFD (Computational Fluid Dynamics) tests and analysis has been performed for a Slocum glider.

The purpose of these tests is to evaluate which CFD code can predict more accurately the drag force on the glider, and, which turbulence model is most appropriate for estimating the drag force.

The CFD results are compared with the results from the drag measurements and self-propulsion experiments which were conducted at the MI (Marine Institute) Flume Tank with Brian Claus' folding-propeller Slocum glider in October and November 2009.

As part of the project which requires the installation of a hydro-acoustic monitoring system on an ocean glider, the CFD tools can be used to assess the impact on the hydrodynamic properties of the glider when the hull is modified by adding new sensors.

2 NUMERICAL MODEL

2.1 CFD Code

The two CFD packages ANSYS-CFX and ANSYS-FLUENT are examined in these tests.

Since version 11 of ANSYS, these two CFD codes are incorporated within the ANSYS-WORKBENCH suite; the most recent version is 12.1.

The conversion from a vehicle geometry file (CAD file) to a mesh file (which defines the grid on which the calculations will take place) can easily be handled within the ANSYS-WORKBENCH environment. However, if there is a need for an advanced meshing methodology to produce a block mesh or a hexagonal mesh, a third party conversion program such as ICEM-CFD® or HyperMesh® is recommended.

As a general assessment of the two CFD codes, CFX has a user-friendly interface and shows good performance for turbo-machinery systems. FLUENT has a fine numerical scheme and is widely used by the ship-building industry.

NRC-IOT has a license for ANSYS-STRUCTURE, ANSYS-Modeler and ANSYS-Mesh but no licenses for either CFX or FLUENT.

2.2 Turbulence Models

The ANSYS CFX brochure entitled "Innovative Turbulence Modeling: SST Model in ANSYS CFX" [1] provides the following background information on turbulence modeling.

> "The standard k-ε model is used in the prediction of most turbulent flow calculations because of its robustness, economy and reasonable accuracy for a wide range of flows. However, the model performs poorly when faced with non-

equilibrium boundary layers. It tends to predict the onset of separation too late as well as to under-predict the amount of separation. Separation influences the overall performance of many devices, such as diffusers, turbine blades and aerodynamic bodies. Separation also has a strong influence on other effects, such as wall heat transfer and multi-phase phenomena. Predicting reduced separation usually results in an optimistic prediction of machine performance. In some applications, this can have dangerous consequences, a notable example being the prediction of wing stall on airplanes.

To solve this problem, new models have been developed. One of the most effective is the shear stress transport (SST) model of Menter [2]. The model works by solving a frequency-based turbulence model (k–ω) at the wall and uses a k-ε turbulence model in the bulk flow. A blending function ensures a smooth transition between the two models. The SST model performance has been studied in a large number of cases. In a NASA Technical Memorandum, [3], SST was rated the most accurate model for aerodynamic applications."

Further information on the k-ε and k–ω and SST turbulence models is described below.

•Two-equation turbulence models

Two-equation turbulence models are one of the most common type of turbulence models. Models such as the k-epsilon model and the k-omega model have become industry standard models and are commonly used for most types of engineering problems. By definition, two-equation models include two extra transport equations to represent the turbulent properties of the flow. This allows a two-equation model to account for fluid-history effects such as convection and diffusion of turbulent energy.

•The k-epsilon model

This is a two-parameter eddy-viscosity-concept model where 'k' is a measure of the kinetic energy of the turbulence, and, 'ε' is a measure of the rate of dissipation of energy, which is contained in the turbulent eddies. Here 'ε' is the parameter which determines the scale of the turbulence, either the length-scale or the time-scale.

• The k-omega model

Again this is two-parameter eddy-viscosity-concept model where 'k' is a measure of the kinetic energy of the turbulence, and, 'ω' is the specific dissipation rate of turbulent kinetic energy, that is, the rate of dissipation per unit turbulent kinetic energy.

• SST models

Shear-stress transport (SST) models combine several desirable elements of existing two-equation models. An SST model modifies the turbulent eddy viscosity function to improve the predictions for separated flows. Two-equation models generally under-predict the retardation of the flow within the boundary layer, and, the separation of the boundary layer, due to adverse pressure gradients. This is a serious deficiency which leads to an underestimation of the effects of the viscous-

inviscid interaction which generally results in too optimistic performance estimates for streamlined aerodynamic and hydrodynamic bodies. The reason for this deficiency is that two-equation models do not account for the important effects of transport of the turbulent stresses; the SST models include those effects.

However, those fully turbulent models could not show a sufficient performance when the flow is under a transient region. In order to describe the transient flow better, a couple of transition models were developed recently. Engineering transition predictions are based mainly on two modeling concepts. The first is the use of low-Reynolds number turbulence models. The second approach is the use of experimental correlations. ANSYS-CFX and ANSYS-FLUENT have the "Transition" turbulence model based on the second approach. The "Transition" turbulence model is called the "Transition γ-θ model" in CFX and "SST transition model (4 equation.)" in FLUENT**.** The following description is for the transition γ-θ model. [4]

- **The transition γ-θ model (also known as SST transition model or 4 equation transition model)**

  The transition γ-θ model introduces two additional parameters which relate the turbulence intensity, Tu, in the free-stream to the momentum-thickness Reynolds number, Re_θ, at transition onset. ANSYS has developed a locally formulated transport equation for the intermittency, γ, which can be used to trigger transition. The full model is based on two transport equations, one for the intermittency and one for the transition onset criteria in terms of momentum thickness Reynolds number. A new empirical correlation (Langtry and Menter) has been developed to cover standard bypass transition as well as flows in low free-stream turbulence environments. These two parameters are formulated together with the SST turbulence model (SST k–ω model) for a wide range of transitional flows. As a result, 4 equations are used to describe the flow pattern in this "Transition" model.

In this study the "SST k-ω" turbulence model and the laminar-to-turbulent "Transition" turbulence model were examined. In practice the glide speed of an ocean glider is about 0.2 to 0.5 m/s. In this region, the Reynolds Number is around $5x10^5$ based on vehicle length. The SST k-ω model shows a good performance for the 2D hydrofoil problem and general problems associated with ships and submarines. The transition model is recently developed to better describe the transient flow by adding an intermittency parameter. In the case of an ocean glider, considering the range of Reynolds Number experienced during gliding, the concept of the use of a transition model is quite suitable in comparison with the use of a fully-turbulent model which might be required for bodies which experience higher Reynolds Numbers.

2.3 Grid system

2.3.1 Background information on types of grids

In 3D a structured grid is a space-filling tessellation of rectilinear parallelepipeds (e.g. bricks). Grids of this type are used in finite element analysis as well as finite volume methods and finite difference methods. Since the derivatives of field variables can be conveniently expressed as finite differences, structured grids mainly appear in finite difference methods.

In 3D an unstructured grid is a tessellation of a part of Euclidean space by simple shapes, such as triangles or tetrahedral, in an irregular pattern. Grids of this type may be used in finite element analysis when the input to be analyzed has an irregular shape. Unlike structured grids, unstructured grids require a list of the connectivity which specifies the way a given set of vertices make up individual elements.

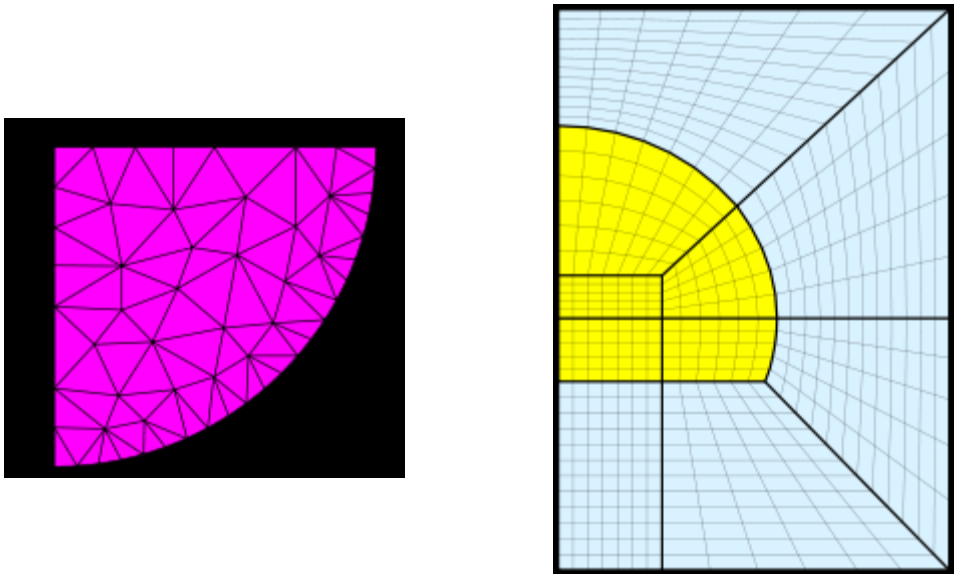

Figure 1. On the left is an example of an unstructured grid and on the right a structured grid

2.3.2 Which type of mesh is used in the ANSYS CFD packages?

ANSYS-CFX and ANSYS-FLUENT have good flexibility in the use of different types of mesh. Both of these codes support structured grid and unstructured grids. However, each of them was developed under the different backgrounds. ANSYS-CFX was developed based on an unstructured grid in order to handle the complex geometry of turbines and rotary machinery efficiently. ANSYS-FLUENT was developed based on a structured grid in order to increase the calculation performance and reduce memory consumption for general problems. Two CFD codes have been improving their mesh flexibilities as indicated below.

> "ANSYS CFX software solves the three-dimensional Navier-Stokes equations on unstructured multi-block grids for both compressible and incompressible flows.

ANSYS CFX offers a wide range of turbulence models, from the standard k-ε model to second moment closure (SMC) and large eddy simulation (LES). SST (shear stress transport), one of the most effective models in ANSYS CFX, has been well tested for accuracy. In addition, a laminar-to-turbulent flow transition model for the SST model is now available."

"The ANSYS FLUENT code provides mesh flexibility via unstructured meshes. Combinations of elements in a variety of shapes are permitted such as quadrilaterals and triangles for 2D simulations and hexahedra, tetrahedra, polyhedra, prisms and pyramids for 3D simulations. Meshes can be created using ANSYS or third-party meshing products and, in the case of polyhedra, via automatic cell agglomeration directly within ANSYS FLUENT software. Turbulence models range from one-equation turbulence model up to Differential Reynolds Stress models (DRSM), including large eddy simulation (LES) and the more economical detached eddy simulation (DES) turbulence models. Innovative new models such as those for predicting laminar-to-turbulent flow transition and the novel scale-resolving Scale-Adaptive Simulation™ (SAS) model for flows in which steady-state turbulence models are insufficient are also available."

2.3.3 Grid and boundary condition

In this study a tetrahedral mesh was formed on the outer surface of the hull. Seven prismatic layers are stacked onto the surface mesh. The thickness of the first prismatic layer is set to 2 mm corresponding to a value of unity for the boundary layer parameter y+. The definition of y+ is shown in equation 1; note that y+ is a non-dimensional quantity. For the laminar sub-layer, the general recommended y+ value is between 1 and 5 [5]. Here

$$y^+ = \frac{u_* y}{\nu} \tag{1}$$

where u* is the friction velocity [m/s], 'y' is the distance to the nearest wall [m], and, ν is the kinematic viscosity of the fluid.

For reliable results, the grid must be fine enough to resolve the important features of the flow, including sufficient details within the boundary layer to be able to integrate the shear stress in order to obtain the contribution of the skin friction. For that reason, in these tests, the y+ value is used to determine the grid sizing parameter. From a numerical perspective, when comparing the results from different CFD codes, one must identify the uncertainties due to (i) the use of different computational grids, (ii) definition of the boundary conditions, (iii) convergence of the solution, and, (iv) the effect of different numerical schemes which are used to implement the same turbulence model.

A photograph of a Slocum glider is shown in Figure 2 and the general specifications are summarized in Table 1 [6]. The numerical model of Slocum glider is simplified as shown in Figure 3. The tail boom, vertical rudder and antenna pod (on top of the rudder)

were removed in order to simplify the mesh and to reduce the computation time. The wing itself is modeled as a flat plat 3 mm thick; the mounting bracket and thus the junction line between the fuselage and main-wing is also simplified. In order to reduce the computational cost, a half model is used and symmetry boundary condition is applied in the vertical plane. Figure 4 shows the boundary conditions for this study.

Figure 2. Picture of Slocum glider

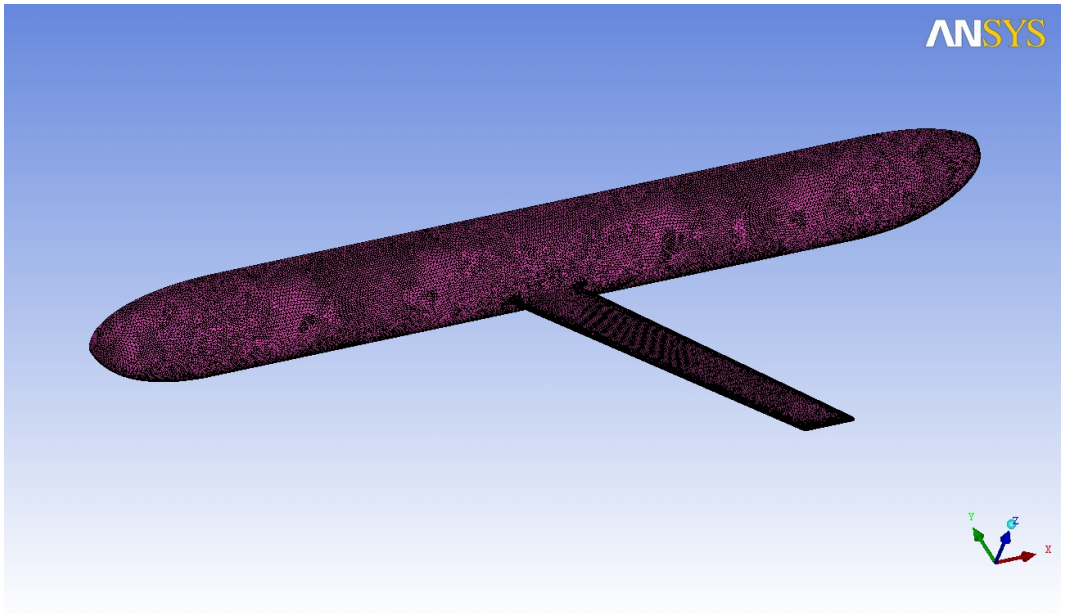

Figure 3. Simplified geometry and surface mesh of Slocum glider

Table 1. General specification of Slocum glider

Weight	52 kg
Hull Diameter	21.3 cm
Vehicle Length	1.5 metre
Speed	0.4 m/sec horizontal average
Depth Range	4 to 200 metre (coastal model) or 1000 metre (deep-water model)

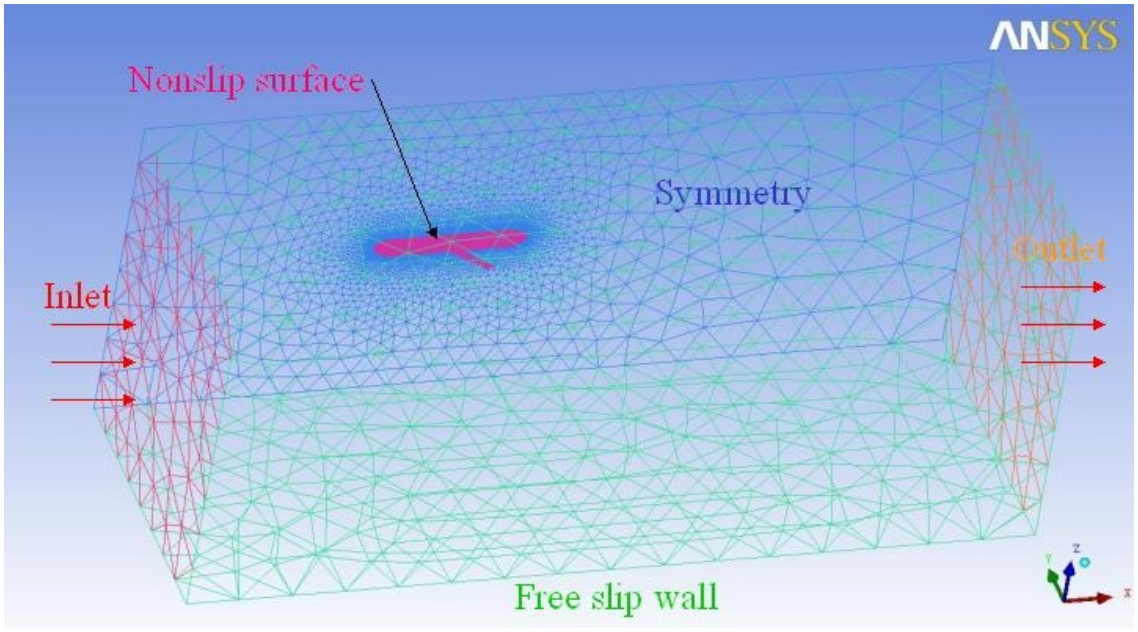

Figure 4. Boundary condition for Slocum glider

Table 2 provides detailed information about the grid system used. Table 3 shows the statistics of the mesh; these values are related to the quality of the grid. Figures 5 to 7 show the volume mesh within the fluid domain. Around the body surface, seven prismatic layers are shown.

Table 2. Mesh information

Nodes	Elements	Tetrahedra	Wedges	Pyramids	Hexahedra	Polyhedra
492892	1848808	1375892	466797	6119	0	0

Table 3. Mesh statistics

Minimum Face Angle (degree)	Maximum Face Angle (degree)	Maximum Edge Length Ratio	Maximum Element Volume Ratio	Connectivity Range	
6	164	9.4	317	1	72

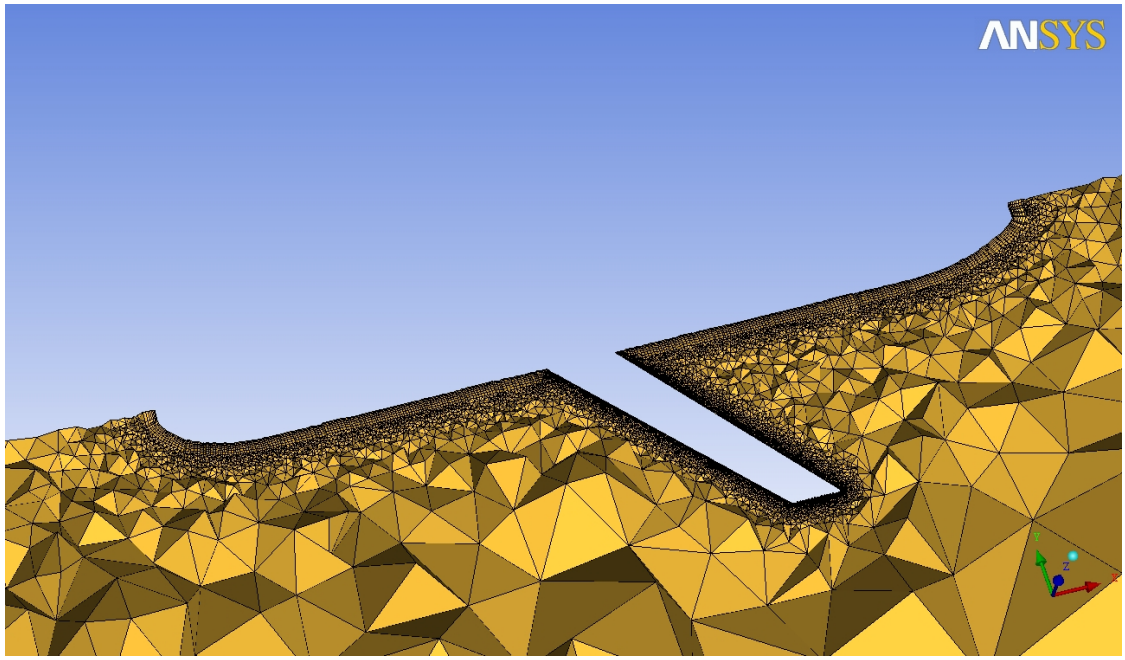

Figure 5. Cut-plan of volume mesh around Slocum glider

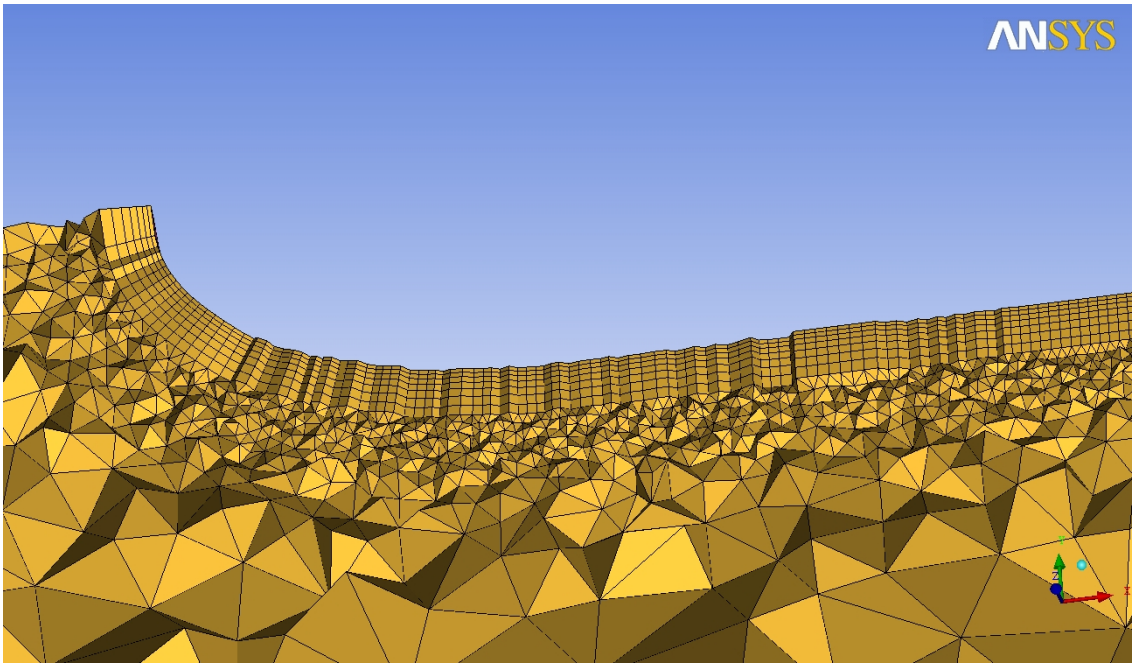

Figure 6. Cut-plan of volume mesh around the cylindrical body

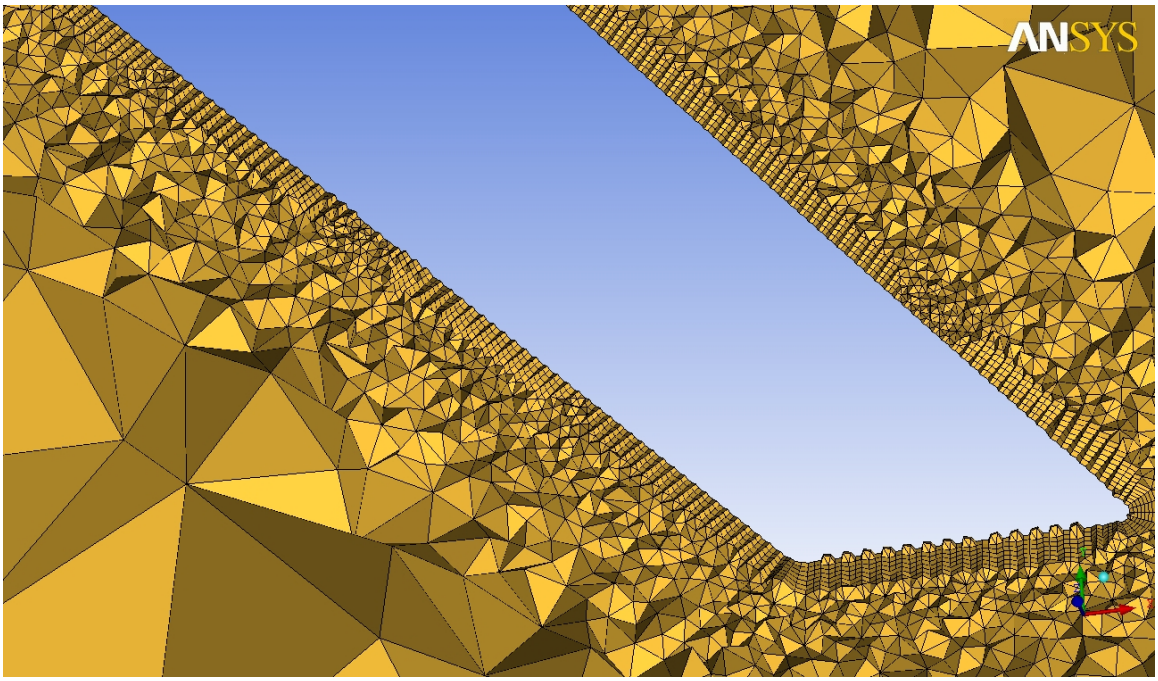

Figure 7. Cut-plan of volume mesh around the main wing

3 SIMULATION RESULT

3.1 Drag Force

Full scale drag and propulsion tests were performed at the Marine Institute's Flume Tank in October and November 2009. This facility has a test section 8 m wide by 4 m deep by 22.5 m long; it is capable of generating steady flow speeds from about 0.1 to 1 m/s. These tests were performed to measure the hydrodynamic drag on the glider and to evaluate its self-propulsion abilities [6]. Table 4 shows a comparison of the CFD predictions with the drag measurements for two flow speeds, 0.3 and 0.6 m/s; the predictions are from CFX and FLUENT, for the two turbulence models "SST k-ω" and "Transition". The results are plotted in Figure 8.

Table 4. Drag forces on a Slocum glider

Velocity (m/s)	CFX		FLUENT		Free Running Test (N)
	SST k-ω (N)	Transition (N)	SST k- ω (N)	Transition (N)	
0.3	0.40	0.31	0.50	0.53	0.50
0.6	1.34	1.05	1.80	1.81	1.75

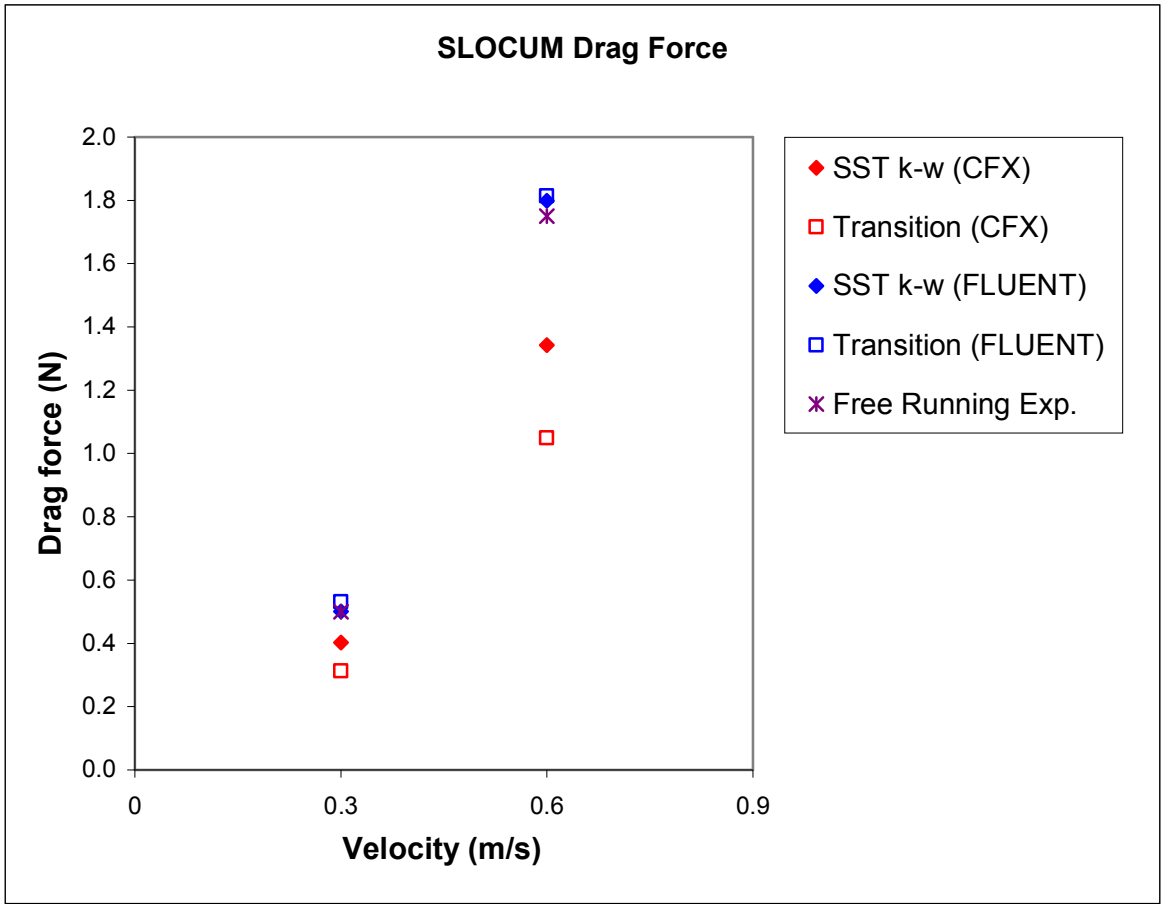

Figure 8. Drag force acting on Slocum glider

Table 5 shows the separate contributions of the wing and hull (main body) to the total drag force. These predictions are from CFX for both the "SST k-ω" and "Transition" turbulence models. At the lower speed of 0.3 m/s, the wing contributes about 20% of the total drag and the hull about 80%. At the higher speed of 0.6 m/s, these contributions change to about 28% and 72% for the wing and hull, respectively.

Table 5. Drag force on wing and body

Velocity	Drag Component	SST k-omega model Force (N)	SST k-omega model Contribution (%)
0.3	Wing	0.07	18
	Main Body	0.33	82
	Total	0.40	100
0.6	Wing	0.35	26
	Main Body	0.99	74
	Total	1.34	100

Velocity	Drag Component	Transition model Force (N)	Transition model Contribution (%)
0.3	Wing	0.07	22
	Main Body	0.24	78
	Total	0.31	100
0.6	Wing	0.32	30
	Main Body	0.73	70
	Total	1.05	100

3.2 Velocity Profile

The following figures are described using the viewpoint as shown in Figure 9. Because a 3D view limits our ability to visualize a detailed value of a plotted quantity, the most interesting two planar views, i.e. vertical and horizontal planes, are selected. In this study, ANSYS CFX-POST is used for the post-processing in order to use the same colour legend and viewpoint. For reference, ANSYS FLUENT contains a similar post-processing ability.

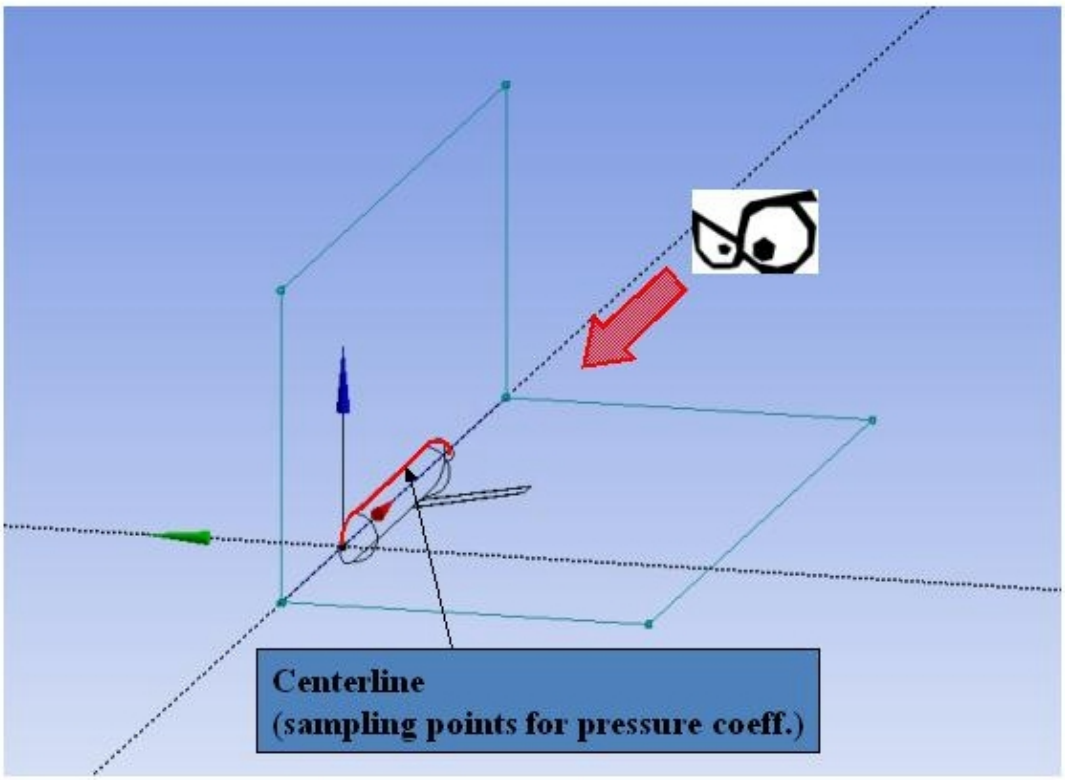

Figure 9. Viewpoint and reference cut-plan

3.2.1 0.3 m/s velocity

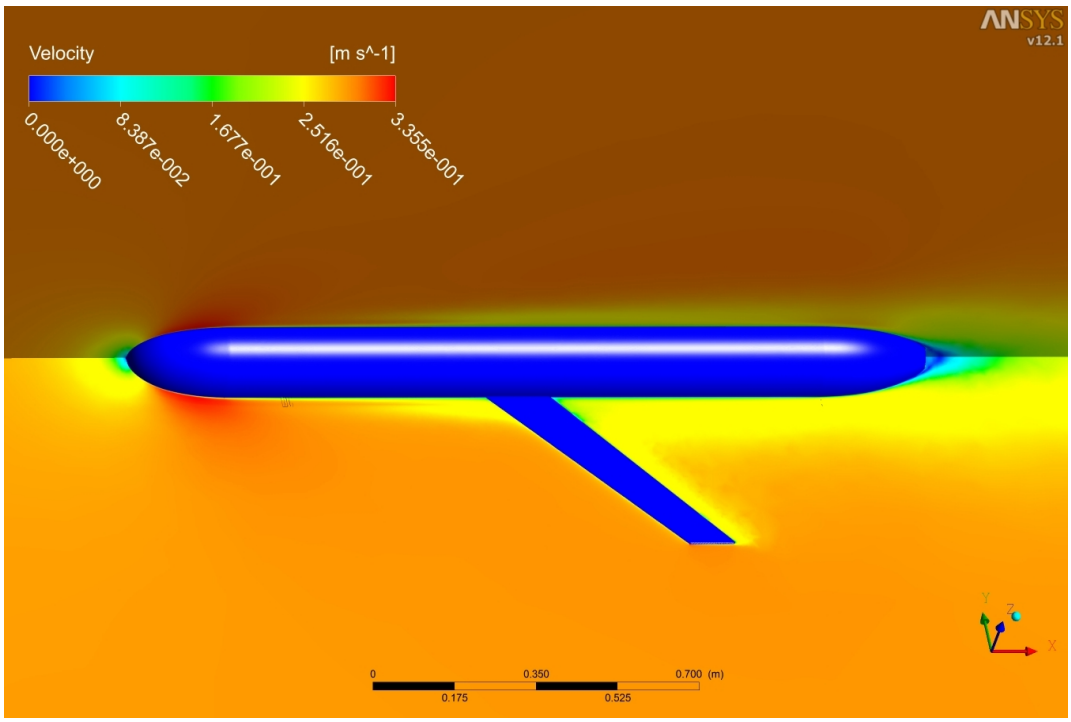

Figure 10. Velocity profile of FLUENT SST k-ω model (at 0.3 m/s)

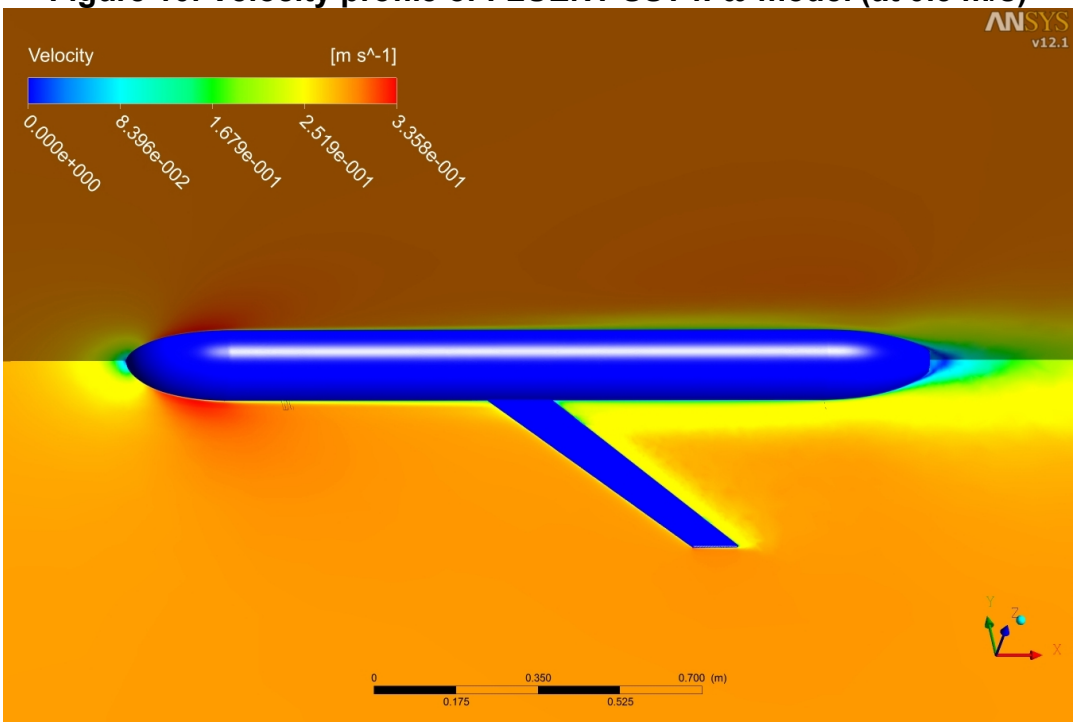

Figure 11. Velocity profile of FLUENT transition model (at 0.3 m/s)

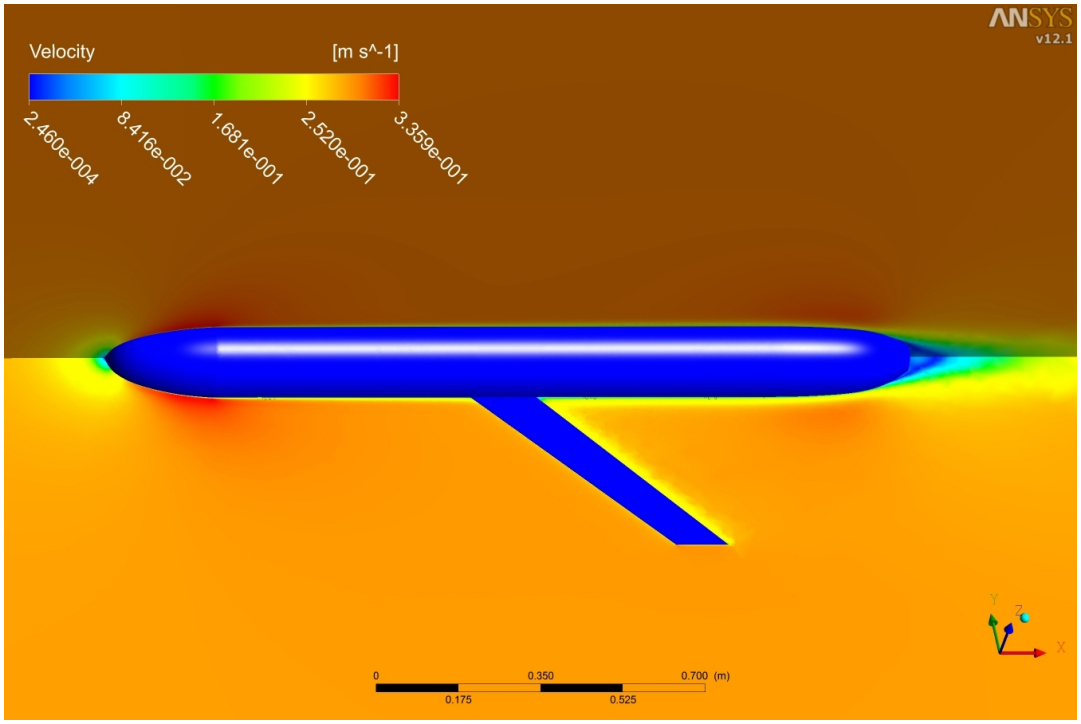

Figure 12. Velocity profile of CFX SST k-ω model (at 0.3 m/s)

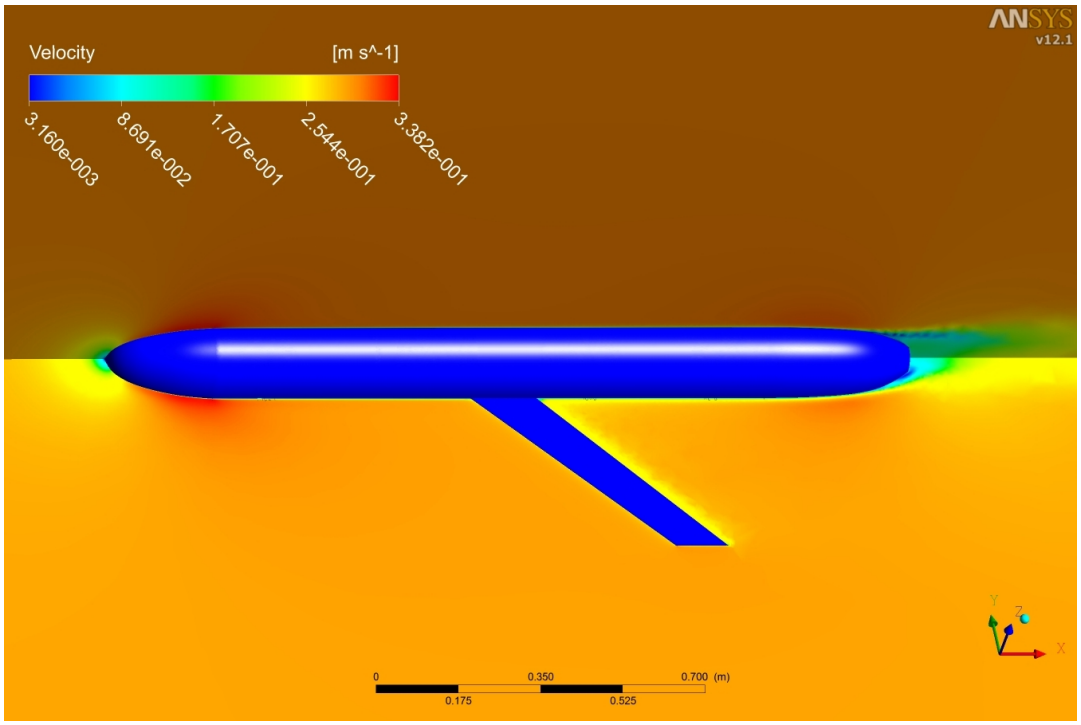

Figure 13. Velocity profile of CFX transition model (at 0.3 m/s)

Figure 10 shows results from using FLUENT with the "SST k-ω" turbulence model when the speed of the approach flow is 0.3 m/s. This figure shows a profile of the flow speed past the glider, using color variations. The legend shows that the speeds in the flow-field vary from zero to about 0.34 m/s; the highest speeds (in red) are along the surface of the hull near the nose. The lowest speeds (in light blue) are in the vicinity of the stagnation point (at the nose), and, in the wake at the aft end of the hull.

The results in Figure 11 are similar to those in Figure 10 but for FLUENT with the "Transition" model, again for an approach-flow speed of 0.3 m/s.

The results from CFX in Figures 12 and 13 are similar to those in Figures 10 and 11 respectively, again for the same two turbulence models and for an approach-flow speed of 0.3 m/s.

3.2.2 0.6 m/s velocity

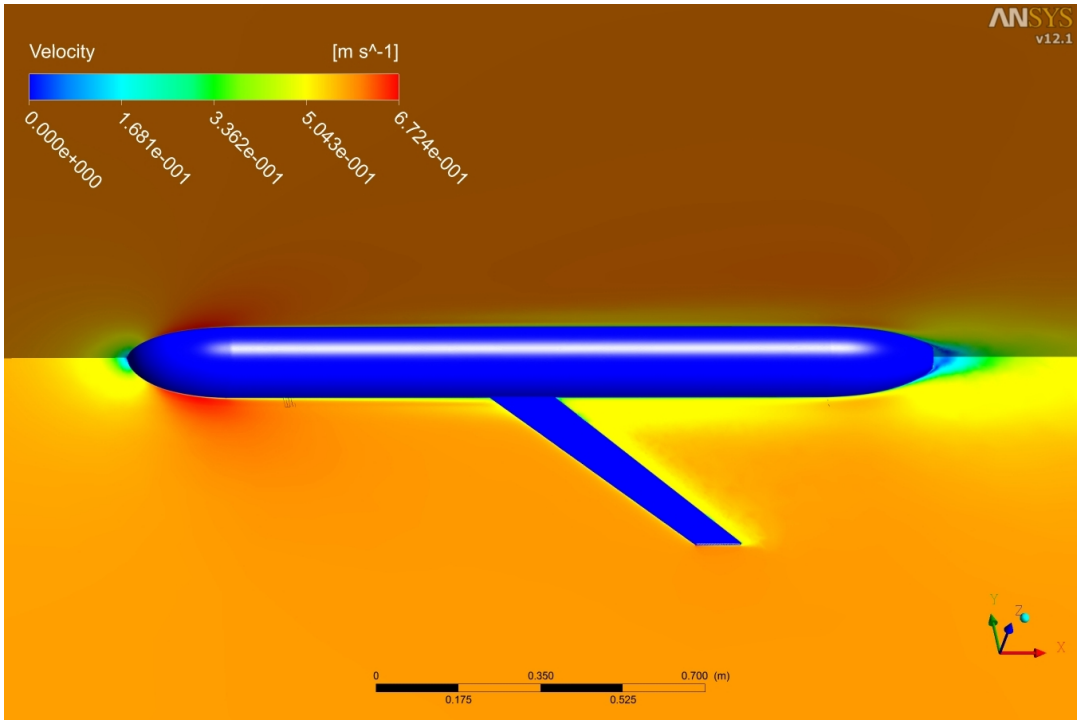

Figure 14. Velocity profile of FLUENT SST k-ω model (at 0.6 m/s)

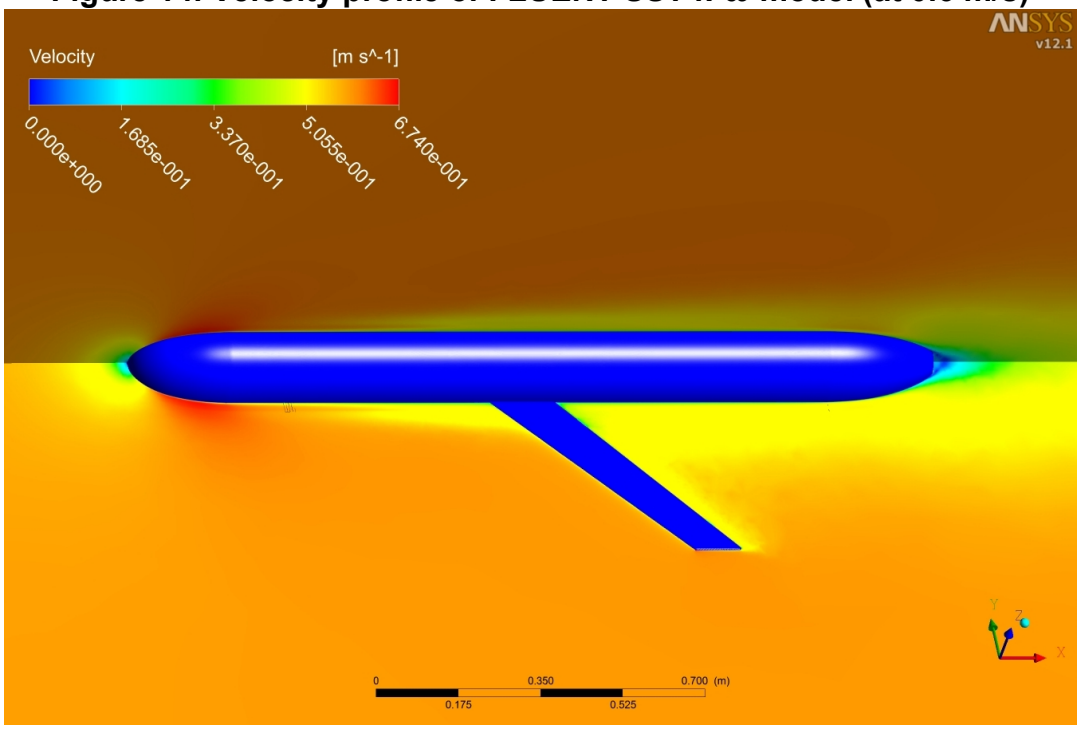

Figure 15. Velocity profile of FLUENT transition model (at 0.6 m/s)

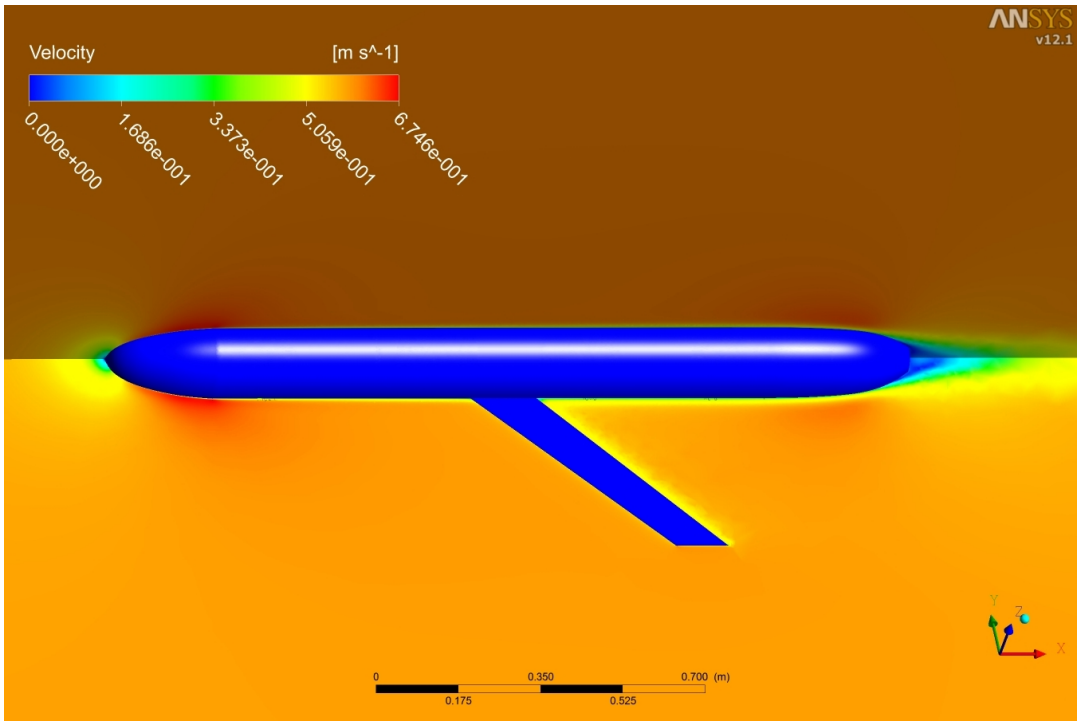

Fig. 16 Velocity profile of CFX SST k-ω model (at 0.6 m/s)

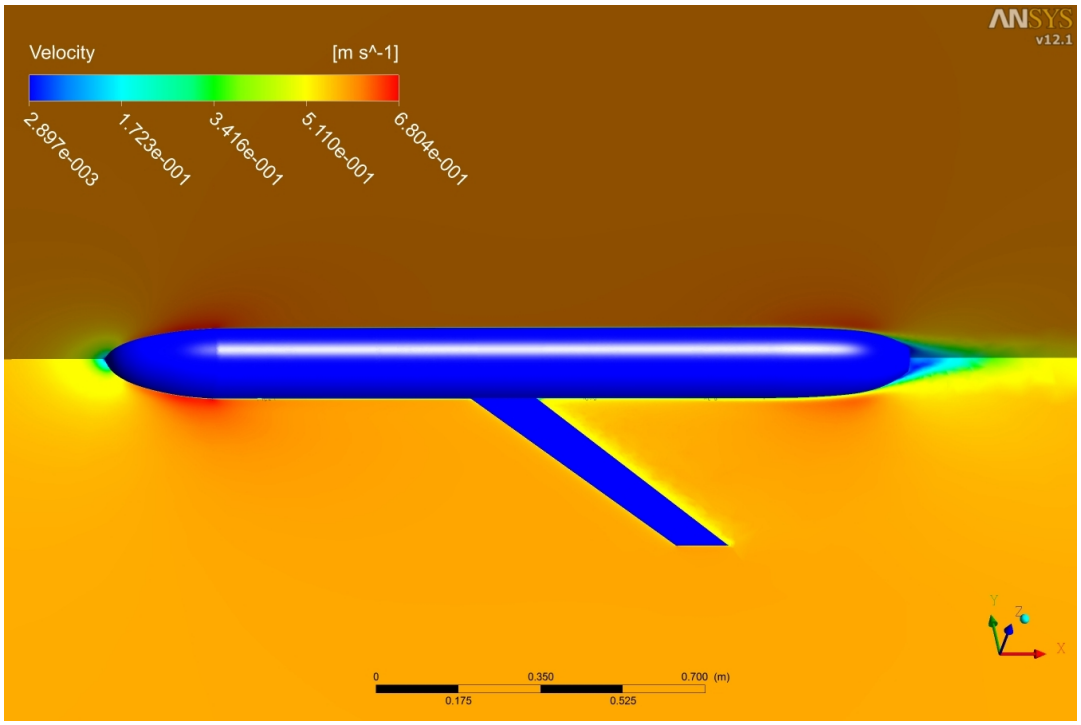

Fig. 17 Velocity profile of CFX transition model (at 0.6 m/s)

The results in Figures 14 and 15 correspond to those in Figures 10 and 11 for FLUENT with the same two turbulence models but for an approach-flow speed of 0.6 m/s. The highest and lowest flow speeds appear in the same places on the hull, and, it appears that the wake region is not spatially larger at 0.6 m/s than at 0.3 m/s.

The results in Figures 16 and 17 correspond to those in Figures 14 and 15 for CFX with the same two turbulence models but for an approach-flow speed of 0.6 m/s. The highest and lowest flow speeds appear in the same places on the hull, and, it appears that the wake region is not spatially larger at 0.6 m/s than at 0.3 m/s. Notice that there is a slight indication of high-speed flow (in red) near where the tapered shape of the tail-section begins on the hull; this indication does not appear on any of the other six flow-speed plots.

3.3 Pressure contours

3.3.1 0.3 m/s velocity

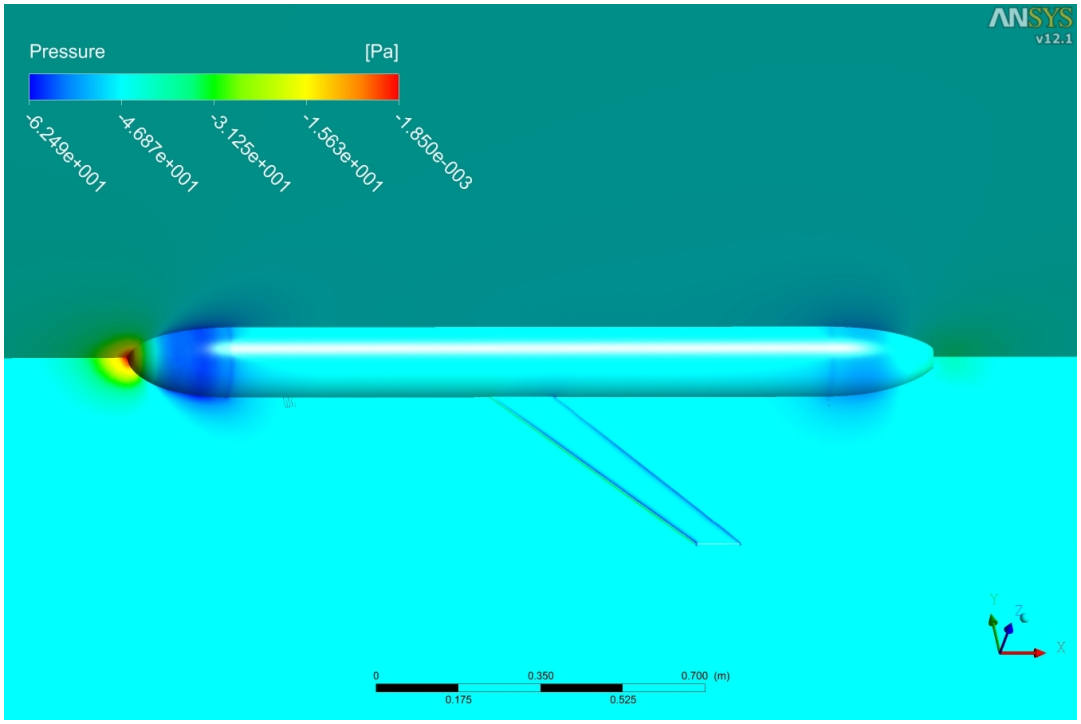

Figure 18. Pressure distribution of FLUENT SST k-ω model (at 0.3 m/s)

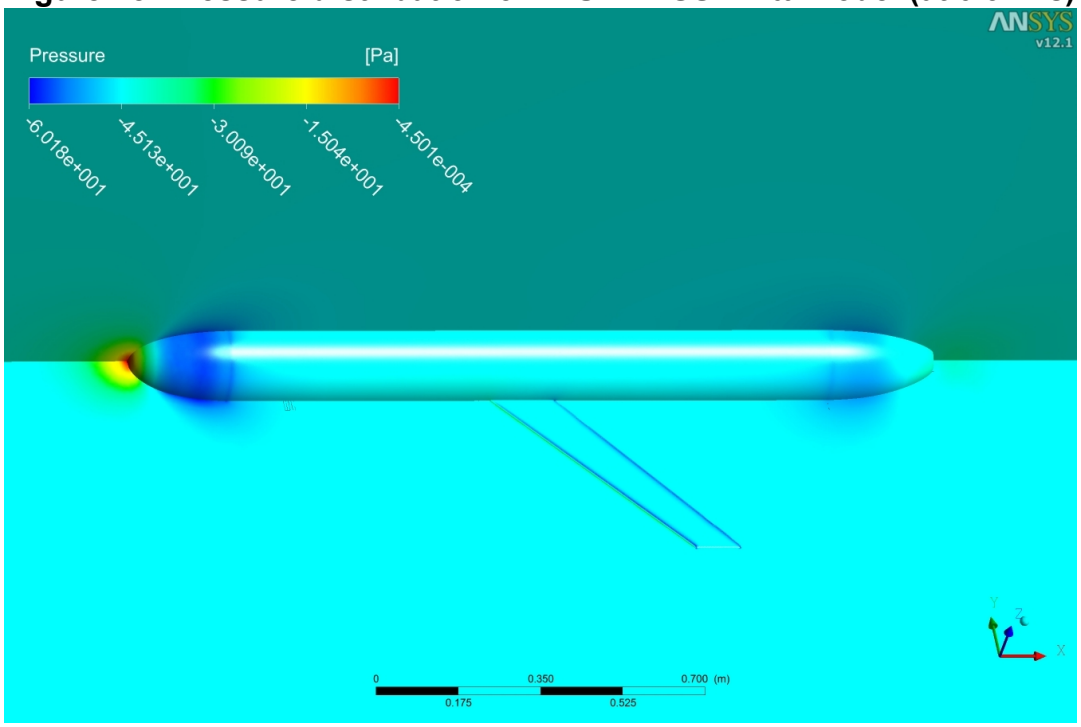

Figure 19. Pressure distribution of FLUENT transition model (at 0.3 m/s)

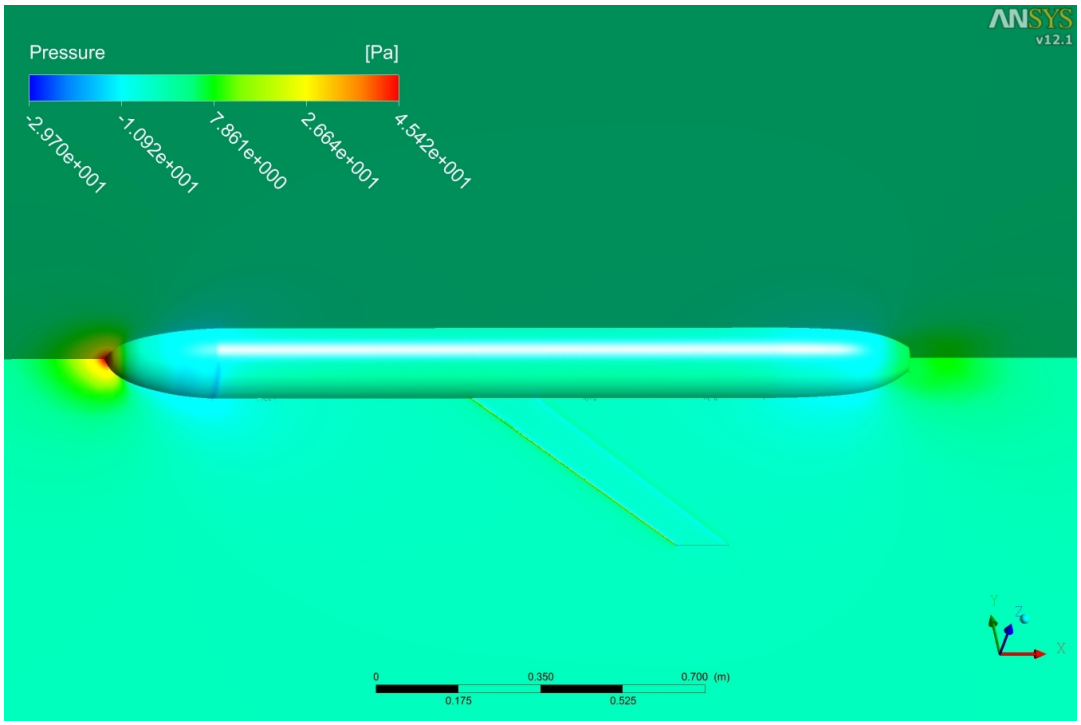

Figure 20. Pressure distribution of CFX SST k-ω model (at 0.3 m/s)

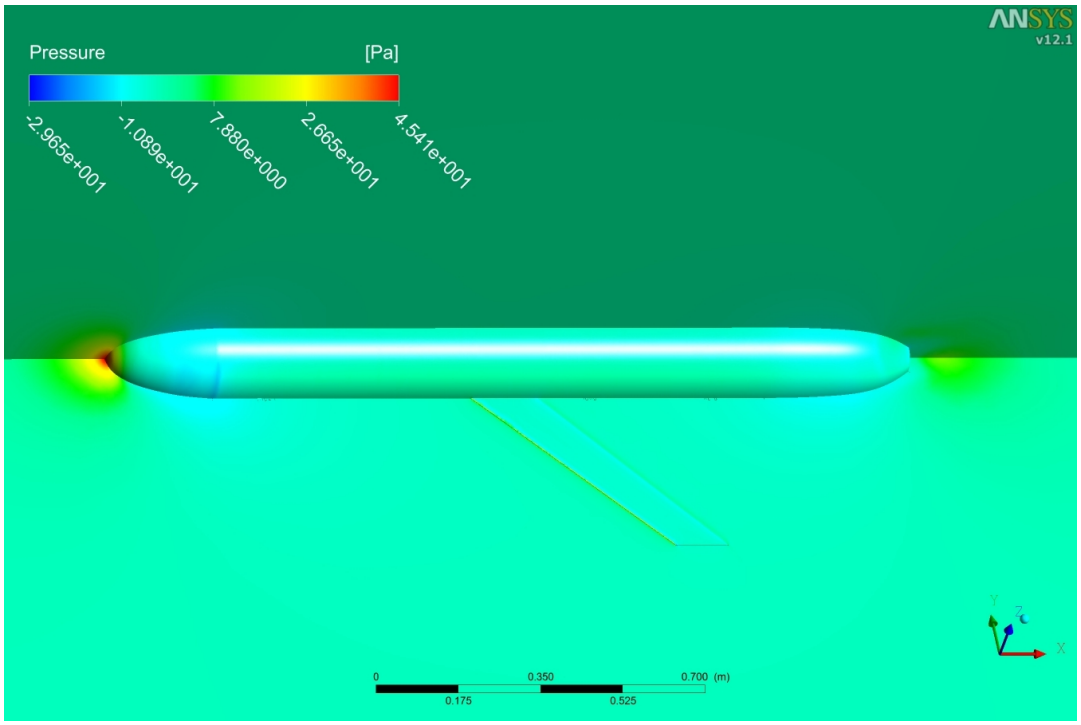

Figure 21. Pressure distribution of CFX transition model (at 0.3 m/s)

Figure 18 shows the distribution of pressure on the surface of glider, and, in the flow-field away from the glider, from using FLUENT with the "SST k-ω" turbulence model when the speed of the approach flow is 0.3 m/s. The legend shows that these pressures vary from zero to about -60 Pa. The smallest negative pressures (in red) occur in the vicinity of the stagnation point at the nose, while the largest negative pressures (in dark blue) occur in the regions of highest flow speed (a) along the nose and (b) at the beginning of the tail-section, as shown previously in the flow-speed plots.

Figure 19 shows results similar to those in Figure 18 but when using FLUENT with the "Transition" turbulence model.

Figure 20 shows the distribution of pressure on the surface of glider, and, in the flow-field away from the glider, from using CFX with the "SST k-ω" turbulence model when the speed of the approach flow is 0.3 m/s. The legend shows that these pressures vary from +45 Pa to about -30 Pa for a range of about 75 Pa. The absolute levels of pressure in this CFX plot are different from those in the FLUENT plots, and, the range of pressures according to CFX is about 1.5 times that predicted by FLUENT.

Apparently FLUENT and CFX use different reference pressures so that explains the observation above that the absolute levels of pressure in the CFX plots are different from those in the FLUENT plots. The reference pressure of FLUENT includes the dynamic pressure at the ambient flow, i.e. $1/2\rho V_\infty^2$. In this case, the dynamic pressure at the ambient flow is about 45 Pa. However, there is a different range in pressure distributions. In order to check the difference between CFX and FLUENT, the pressure distribution of CFX below about -15 Pa is plotted as shown in Figure 22. Figure 22 is the case of “SST k-ω“ turbulence model with CFX. As shown in the figure, the difference is shown in the small local area around shoulder from the nose to main cylindrical hull.

Figure 21 shows results similar to those in Figure 20 but when using CFX with the "Transition" turbulence model.

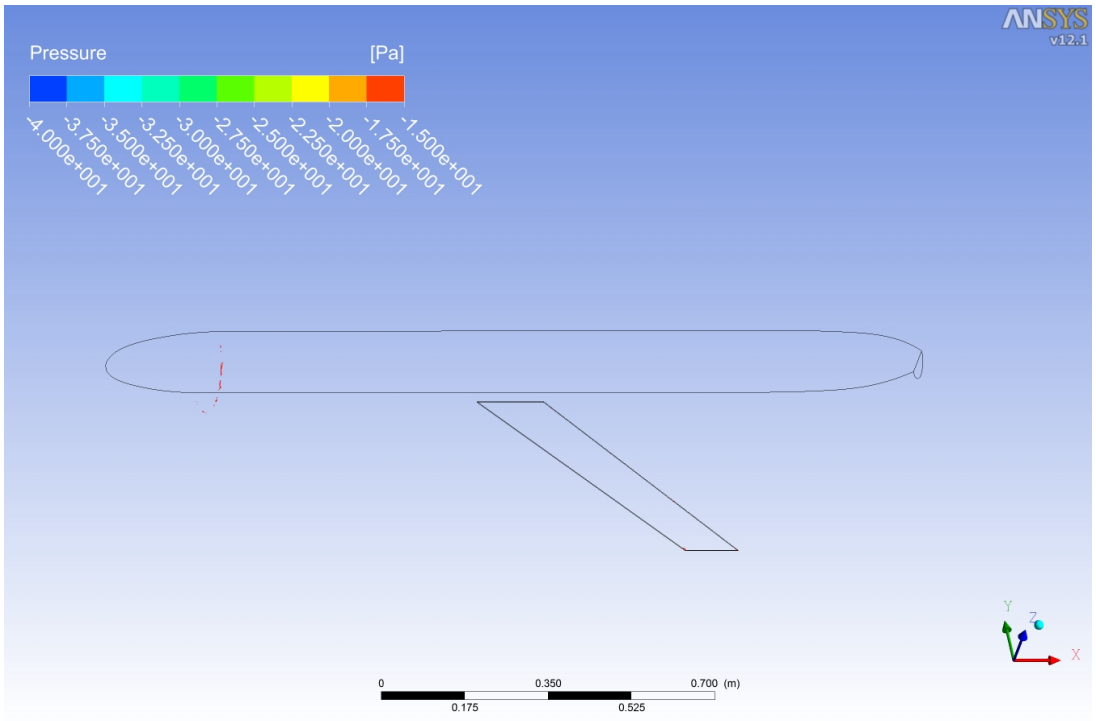

Figure 22. Pressure distribution of CFX SST-kω model below -15 Pa (at 0.3 m/s)

3.3.2 0.6 m/s velocity

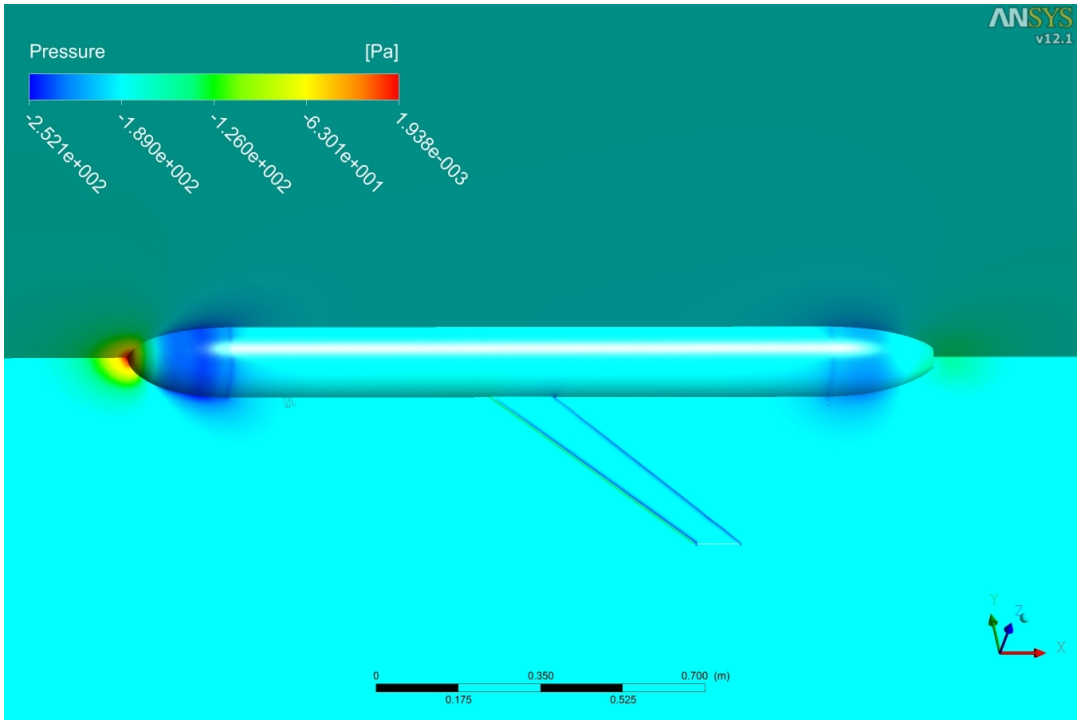

Figure 23. Pressure distribution of FLUENT SST k-ω model (at 0.6 m/s)

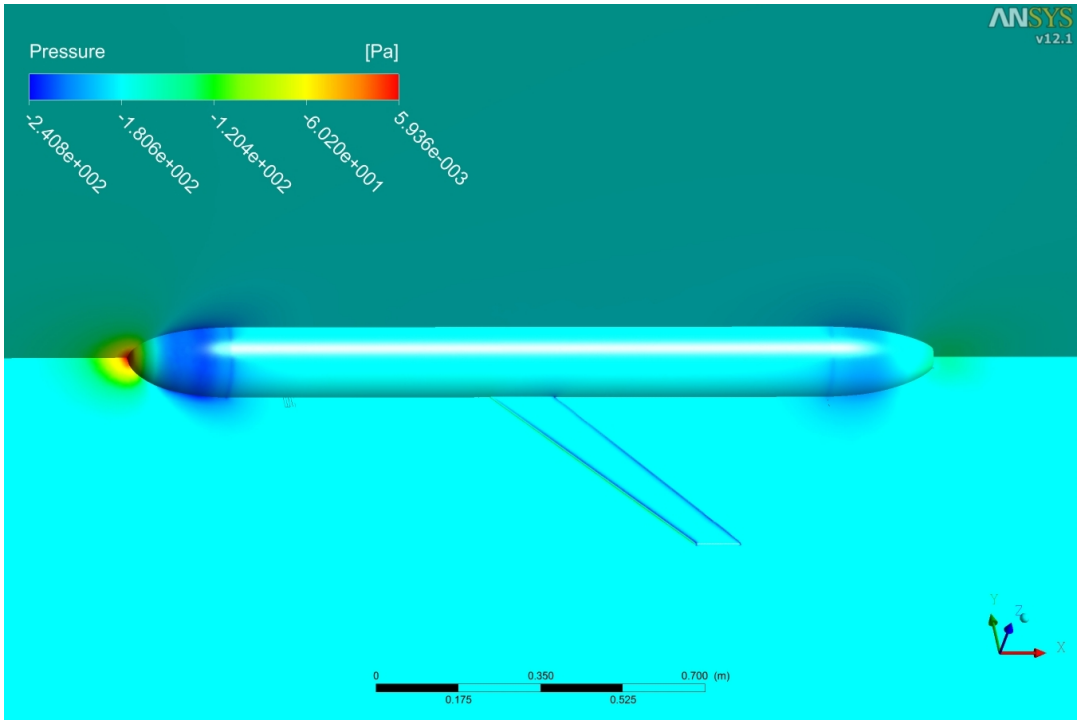

Figure 24. Pressure distribution of FLUENT transition model (at 0.6 m/s)

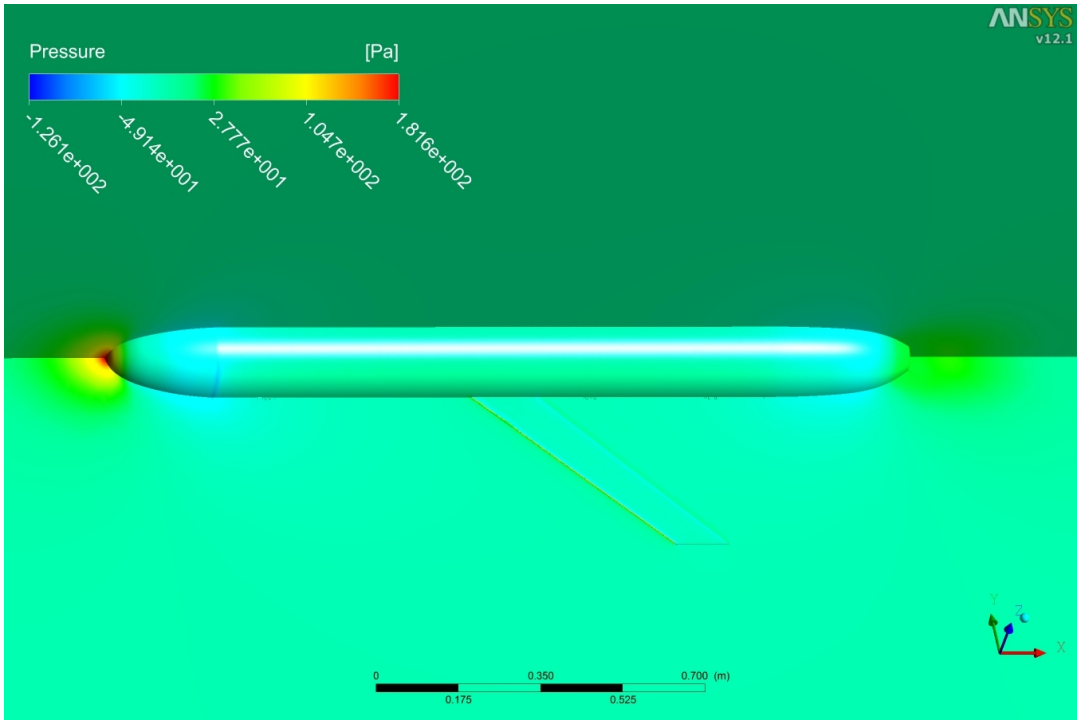

Figure 25. Pressure distribution of CFX SST k-ω model (at 0.6 m/s)

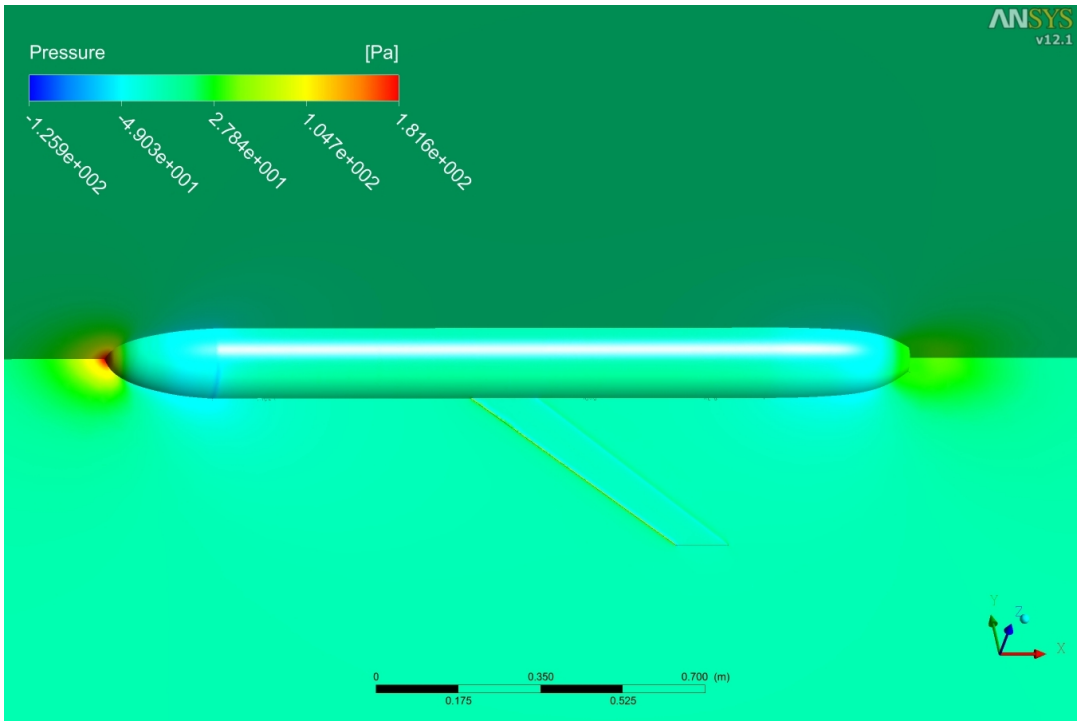

Figure 26. Pressure distribution of CFX transition model (at 0.6 m/s)

Figure 23, like Figure 18, shows the distribution of pressure on the surface of glider, and, in the flow-field away from the glider, from using FLUENT with the "SST k-ω" turbulence model when the speed of the approach flow is 0.6 m/s. The legend shows that these pressures vary from zero to about -252 Pa. The smallest negative pressures (in red) occur in the vicinity of the stagnation point at the nose, while the largest negative pressures (in dark blue) occur in the regions of highest flow speed (a) along the nose and (b) at the beginning of the tail-section, as shown previously in the flow-speed plots.

Figure 24 shows results similar to those in Figure 23 for an approach-flow speed of 0.6 m/s; these pressure-distribution results are from using FLUENT with the "Transition" turbulence model. Here the pressure range from zero to -240 Pa so the range is similar to Figure 23.

Figure 25, like Figure 20, shows the distribution of pressure on the surface of glider, and, in the flow-field away from the glider, from using CFX with the "SST k-ω" turbulence model when the speed of the approach flow is 0.6 m/s. Here the pressures vary from +182 to -126 Pa thus a range of 308 Pa, which is 22% larger range than the results in Figure 23 with FLUENT and the same turbulence model. In this case, the dynamic pressure at the ambient flow is about 180 Pa, which agrees well with the maximum pressure of 182 Pa. The pressure below -60 Pa is shown in Figure 27. As is the case for the approach flow speed of 0.3 m/s shown in Figure 22, the difference appears only in a small localized region near the shoulder between the nose and the main cylindrical hull.

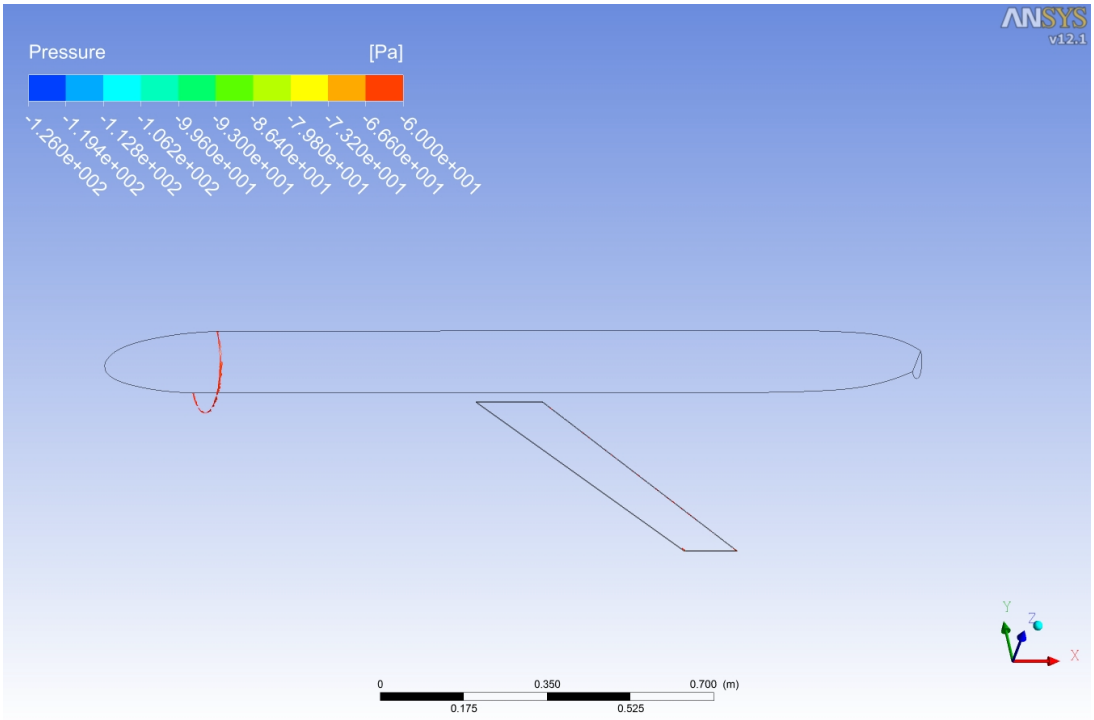

Figure 27. Pressure distribution of CFX SST-kω model below -60 Pa (at 0.6 m/s)

Figure 26 shows results similar to those in Figure 25 for an approach-flow speed of 0.6 m/s; these pressure-distribution results are from using CFX with the "Transition" turbulence model. Here the pressure again ranges from +182 to -126 Pa, so the range is essentially the same as in Figure 25.

3.4 Turbulence kinetic energy

The turbulence kinetic energy (TKE) is defined in the following expression. The TKE is characterised by the measured root-mean-square (RMS) fluctuations of the three orthogonal velocity components (u,v,w). The TKE can be used to indicate how much turbulence is present at any location in the flow-field. For example, if the flow is assumed to be laminar, the TKE value equals zero. A high TKE value means that the flow is highly fluctuating, and thus highly turbulent.

$$TKE = \frac{1}{2}\left(\overline{(u_1')^2} + \overline{(u_2')^2} + \overline{(u_3')^2}\right) \tag{2}$$

where ū is mean value of velocity component u(t) and u' is the fluctuating portion of u(t) and is thus the turbulence term; note that the time-average of u' is zero by definition.

In the "Transition" model, the intermittency parameter is introduced to judge whether the flow is laminar or turbulent. If the simulated flow includes a transient region, the intermittency parameter varies between 0 and 1. If the intermittency parameter is zero, the flow is laminar. If the parameter is more than 1, the flow is fully turbulent. If the flow is transient, the intermittency parameter is between 0 and 1. However, the intermittency parameter can be applied only with “Transition” turbulence model with CFX. In this study, the TKE is used instead of the intermittency parameter. Figure 28 shows the similarity between the intermittency parameter γ and TKE value.

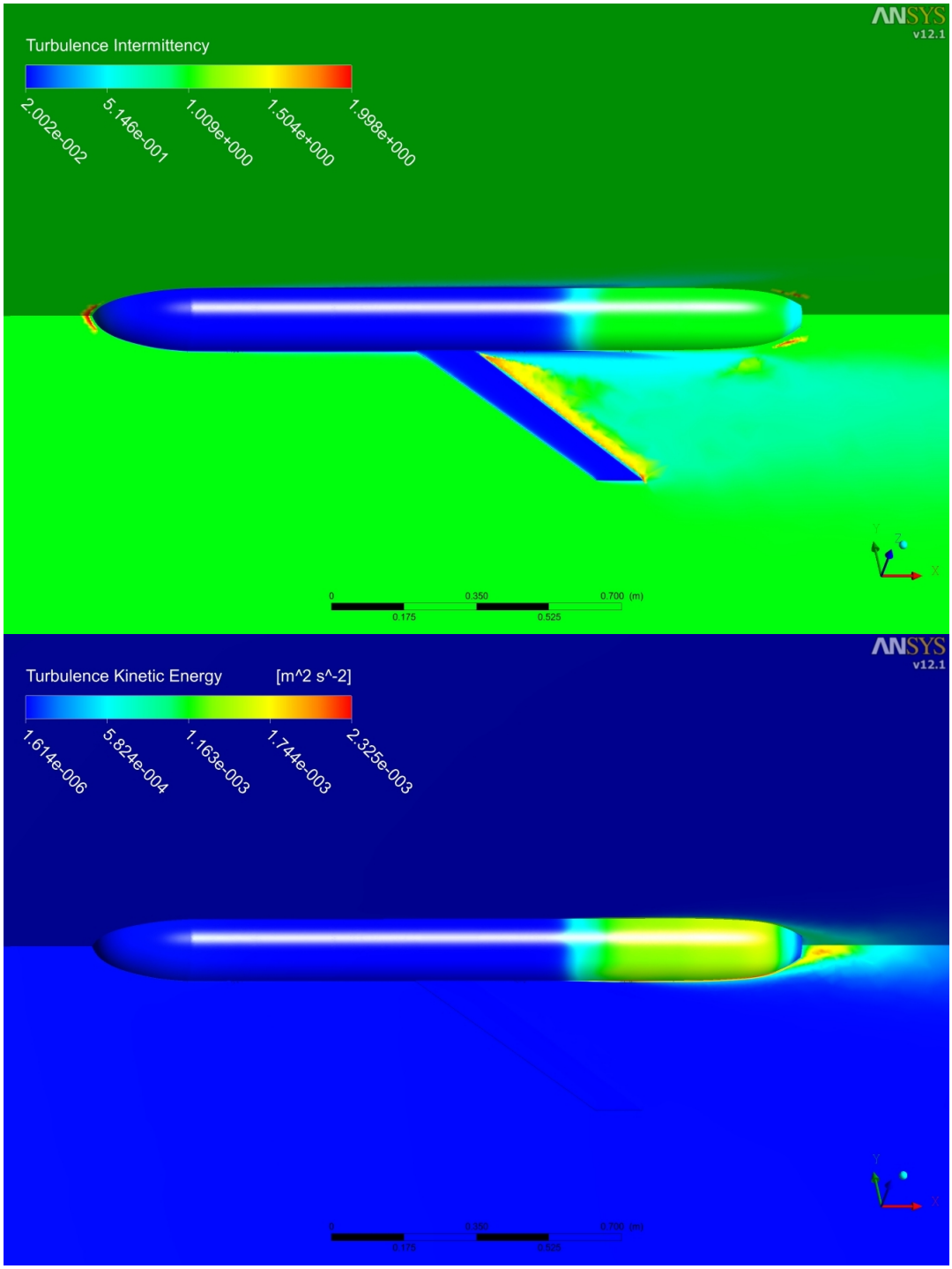

Figure 28. Turbulence intermittency parameter (above) and TKE distribution (below) of Transition model with CFX at 0.6 m/s

3.4.1 0.3 m/s velocity

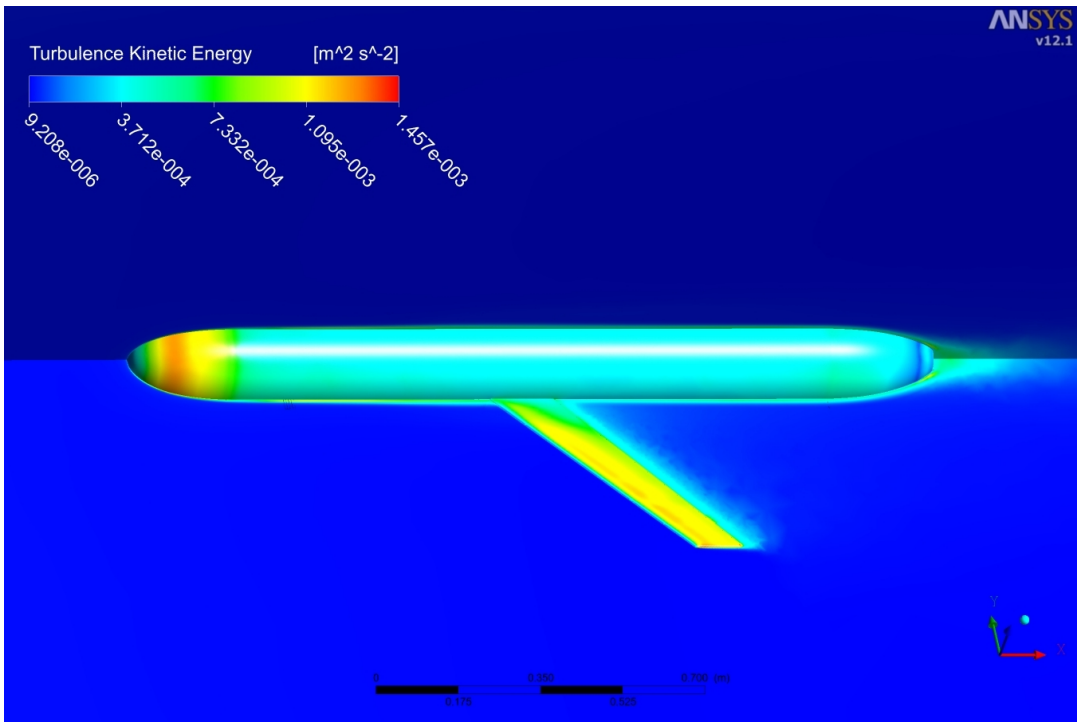

Figure 29. TKE distribution of FLUENT SST k-ω model (at 0.3 m/s)

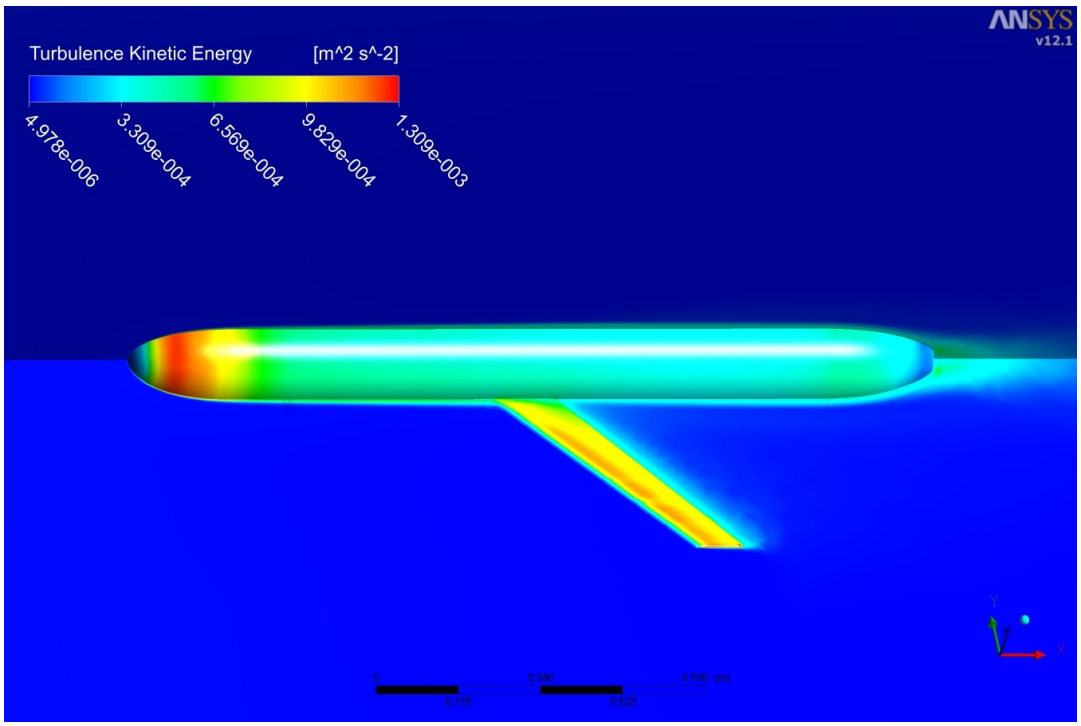

Figure 30. TKE distribution of FLUENT transition model (at 0.3 m/s)

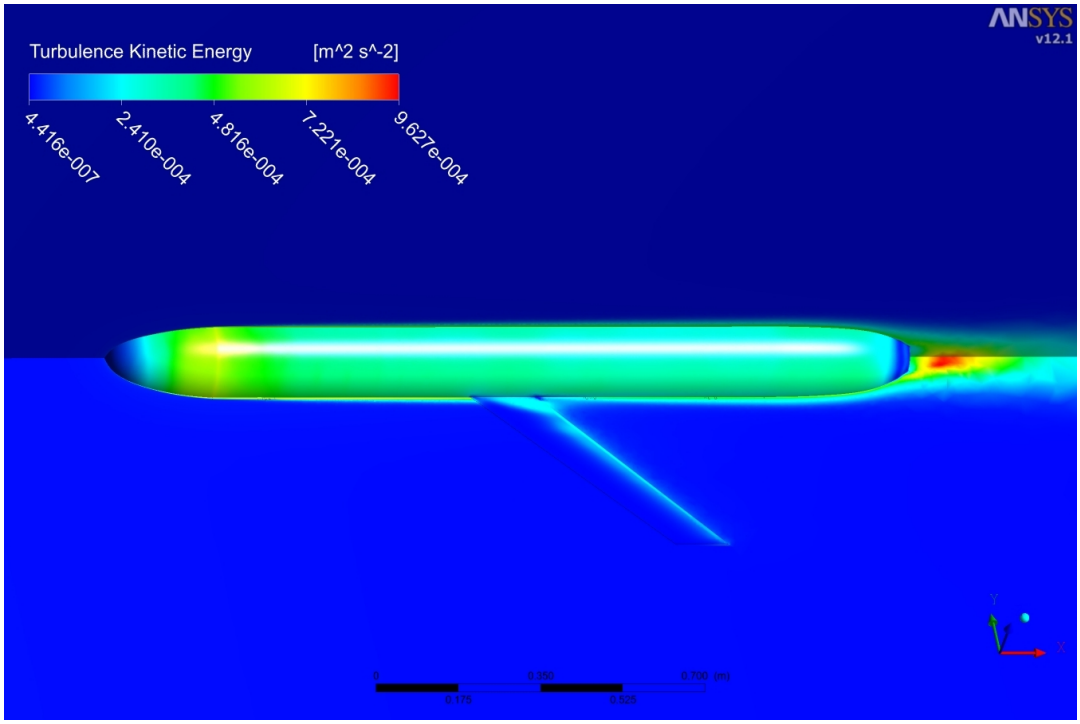

Figure 31. TKE distribution of CFX SST k-ω model (at 0.3 m/s)

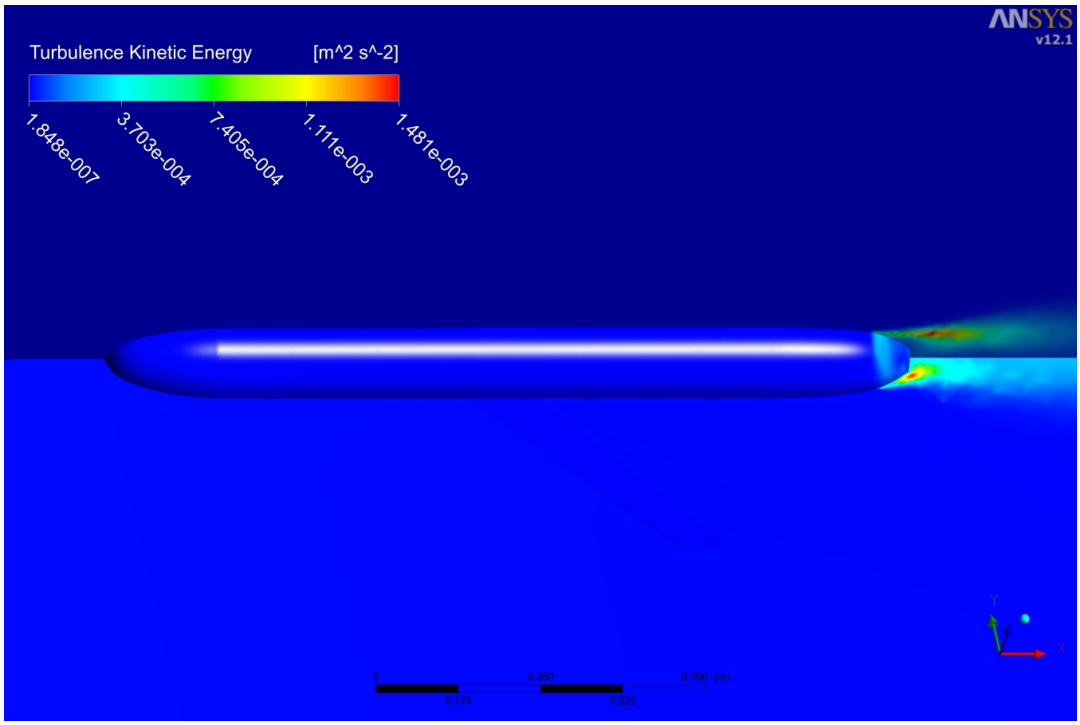

Figure 32. TKE distribution of CFX transition model (at 0.3 m/s)

Figure 29 shows the distribution of TKE on the surface of glider, and, in the flow-field away from the glider, from using FLUENT with the "SST k-ω" turbulence model when the speed of the approach flow is 0.3 m/s. The legend shows that the values of the TKE vary from zero to about +0.0015 $(m/s)^2$. The region of highest TKE (in red) occurs (a) about mid-way along the nose, and, (b) along the outboard leading edge of the wing.

Figure 30 shows results similar to those in Figure 29 but when using FLUENT with the "Transition" turbulence model. The values of the TKE are similar with these two turbulence models over the hull but the "Transition" model seems to show a larger extent of high TKE along the upper surface of the wing. In this case, the “Transition” turbulence model of FLUENT can be considered to handle this region of the fully turbulent flow in a manner similar to the “SST-kω” turbulence model.

Figure 31, like Figure 29, shows the distribution of TKE on the surface of glider, and, in the flow-field away from the glider, from using CFX with the "SST k-ω" turbulence model when the speed of the approach flow is 0.3 m/s. The legend shows that the values of the TKE vary from zero to about 0.00103 $(m/s)^2$ which is only 70% of the range shown in Figure 29. In comparison with Figure 29, Figure 31 is not showing regions of high TKE on the wing. In addition, in Figure 31 the colours in the nose region do not appear as distinct "bands" as they do in Figure 29.

Figure 32 shows results similar to those in Figure 30 but when using CFX with the "Transition" turbulence model. The legend shows that the values of the TKE vary from zero to about 0.0015 which is similar to the range shown in Figures 29 and 30. But the major difference is that the only regions of high TKE are in the vicinity of the aft end of the hull, which is not at all as in Figures 29, 30 and 31. Figure 32 shows that along almost the whole length of the glider, the TKE value is around zero; this indicates that the "Transition" turbulence model of CFX assumes the flow is laminar.

3.4.2 0.6 m/s velocity

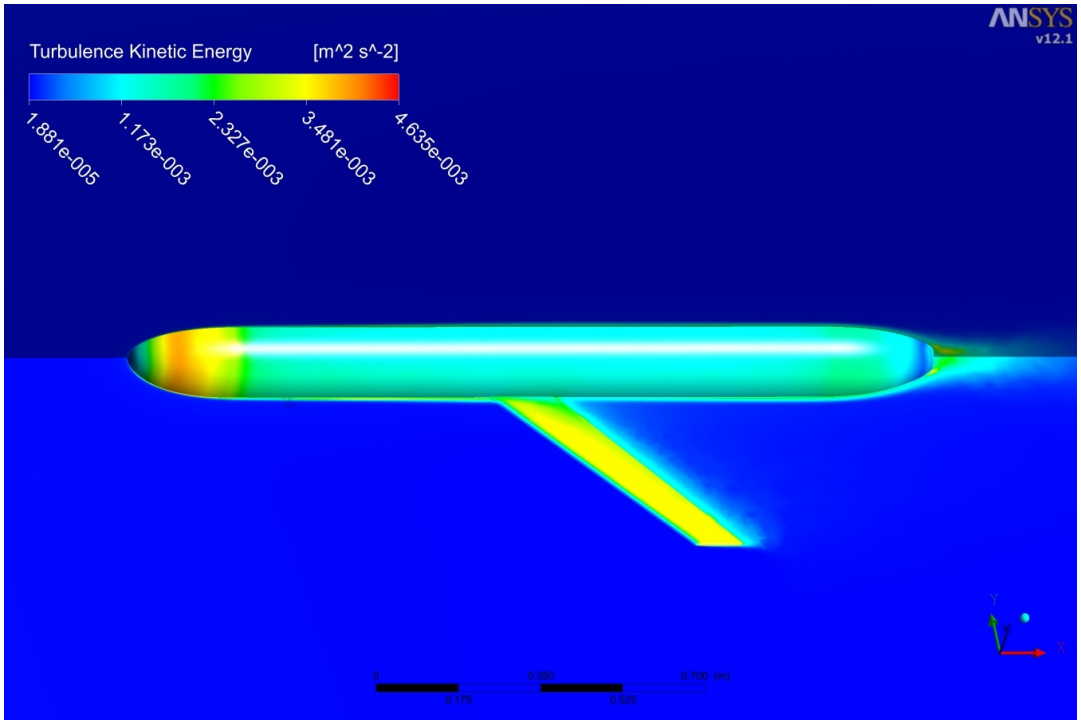

Figure 33. TKE distribution of FLUENT SST k-ω model (at 0.6 m/s)

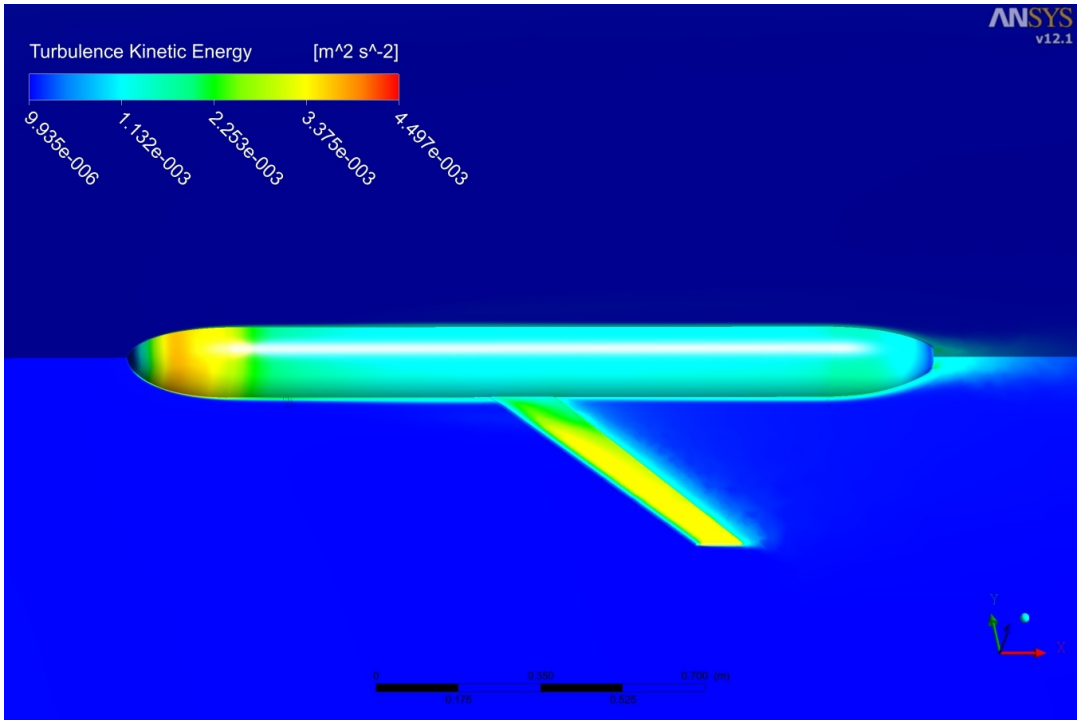

Figure 34. TKE distribution of FLUENT transition model (at 0.6 m/s)

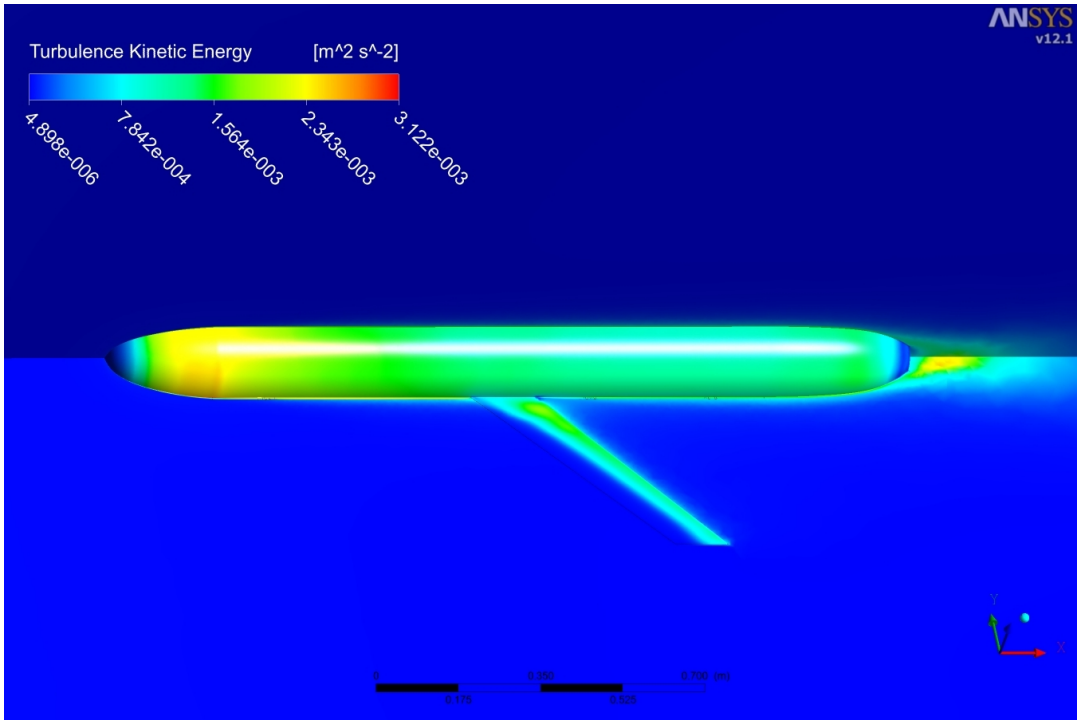

Figure 35. TKE distribution of CFX SST k-ω model (at 0.6 m/s)

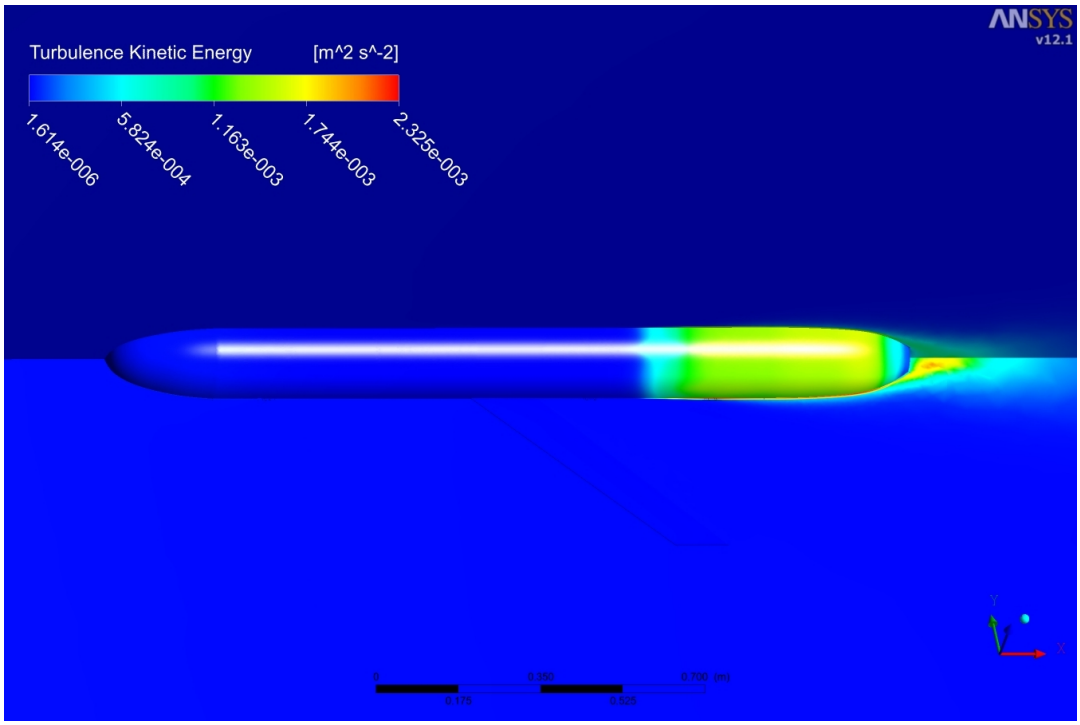

Figure 36. TKE distribution of CFX transition model (at 0.6 m/s)

Figure 33, like Figure 29, shows the distribution of TKE on the surface of glider, and, in the flow-field away from the glider, from using FLUENT with the "SST k-ω" turbulence model, but when the speed of the approach flow is 0.6 m/s. The legend shows that the values of the TKE vary from zero to about 0.0047 $(m/s)^2$. Visually the results are similar to those in Figure 29 so the effect of doubling the speed has not changed the distribution of TKE along the hull or wing.

Figure 34 shows results similar to those in Figure 33 but when using FLUENT with the "Transition" turbulence model, with values of the TKE ranging from zero to about 0.0045 $(m/s)^2$. The values of the TKE are similar with these two turbulence models over the hull but the "Transition" model seems to show a larger extent of high TKE along the upper surface of the wing.

Figure 35, like Figure 31, shows the distribution of TKE on the surface of glider, and, in the flow-field away from the glider, from using CFX with the "SST k-ω" turbulence model, but when the speed of the approach flow is 0.6 m/s. The legend shows that the values of the TKE vary from zero to about 0.0031 $(m/s)^2$ which is about two-thirds of the range shown in Figures 33 and 34 using FLUENT. In opposition to Figures 33 and 34, the region of highest TKE on the wing in Figure 35 is adjacent to the trailing edge, not the leading edge.

Figure 36, like Figure 32, shows the distribution of TKE on the surface of glider, and, in the flow-field away from the glider, from using CFX with the "Transition" turbulence model, but when the speed of the approach flow is 0.6 m/s. The legend shows that the values of the TKE vary from zero to about 0.0023 $(m/s)^2$ which is about half of the range shown in Figures 33 and 34 using FLUENT. As in Figure 36, the two TKE distributions using CFX with the "Transition" turbulence model, the major difference is that the only regions of high TKE are in the vicinity of the aft end of the hull, which is not at all as in Figures 29 to 31 and 33 to 35. Compared with Figure 32 for the lower velocity of 0.3m/s, Figure 36 shows that the laminar flow region where the TKE is about zero becomes shorter; this means that the transition region moves forward at the higher velocity of 0.6 m/s. The change predicted by the increase in the approach flow velocity can be considered to be an overestimation because this rapid change can be observed at the actual transition point. However, CFX shows a possibility to approach the transient flow problem using that CFD code.

Comparing the two “Transition” turbulence model of FLUENT and CFX, CFX shows the transition phenomenon from laminar to turbulent flow clearly. FLUENT shows a consistency with the “SST k-ω” turbulence model, which is basis of the “Transition” turbulence model.

3.5 The reason why the different drag force is estimated differently by CFX and FLUENT

FLUENT and CFX show qualitatively similar results such as velocity profiles, pressure contours and TKE distributions. However, the predicted drag forces are not in agreement with each other. In order to analyze the reason, the total drag force is divided into two components, pressure drag and viscous drag. Tables 6 and 7 show the separate contributions of the pressure (form) drag and the viscous drag to the total drag force. These predictions are from both FLUENT and CFX for both the "SST k-ω" and "Transition" turbulence models.

As shown in Table 6, the “SST k- ω” turbulence model with FLUENT has about 37% of pressure drag and about 62% of viscous drag. In case of the “SST k- ω” turbulence model of CFX, the pressure drag is about 25% and the viscous drag is about 75%. Comparing both CFD codes, the pressure drag of FLUENT is about as twice as that of CFX. In the viscous drag, both CFD codes show similar numerical values.

Table 7 shows the contributions for the “Transition” turbulence model. For FLUENT, the pressure component contributes about 35% and the viscous component contributes about 65%. This result of “Transition” turbulence model of FLUENT is analogous to that of “SST k-ω “ turbulence model. For FLUENT there is only a small difference between the two turbulence models for the case of 0.3 m/s and 0.6 m/s. However, considering the results of CFX, the contribution of the pressure component and viscous component depends on the velocity. At the lower speed of 0.3 m/s, the pressure drag is the dominant component. At higher speed of 0.6 m/s, the viscous drag becomes higher than the pressure drag.

Table 6. Drag force contribution of pressure and viscosity (SST-kω)

Velocity (m/s)	Drag component	FLUENT		CFX	
		Force (N)	Portion (%)	Force (N)	Portion (%)
0.3	Pressure drag	0.18	37	0.09	24
	Viscous drag	0.32	63	0.31	76
	Total Drag	0.50	100	0.40	100
0.6	Pressure drag	0.68	38	0.37	27
	Viscous drag	1.12	62	0.97	73
	Total Drag	1.80	100	1.34	100

Table 7. Drag force contribution of pressure and viscosity (Transition)

Velocity (m/s)	Drag component	FLUENT		CFX	
		Force (N)	Portion (%)	Force (N)	Portion (%)
0.3	Pressure drag	0.17	33	0.21	60
	Viscous drag	0.36	67	0.14	40
	Total Drag	0.53	100	0.35	100
0.6	Pressure drag	0.70	39	0.38	37
	Viscous drag	1.11	61	0.65	63
	Total Drag	1.81	100	1.03	100

In order to compare the results in detail, the pressure coefficients are introduced. The pressure coefficient can be calculated using equation. 3. Usually, at the stagnation point, the pressure coefficient equals 1.

$$C_P = \frac{P - P_\infty}{1/2\rho V_\infty^2} \tag{3}$$

where P is the dynamic pressure in the flow [Pa], P_∞ is the ambient static pressure [Pa], ρ is the fluid density [kg/m3], and, V_∞ is the velocity of the approaching flow.

Figure 37 shows the pressure coefficient along the centerline plane as shown in Figure 9. As shown in Figure 37, the overall tendencies of the various pressure coefficient look similar. However, around the nose part (0.2 m) CFX and FLUENT show quite different results. Also, around the tail part (1.6 m), the two turbulence models of CFX show different values.

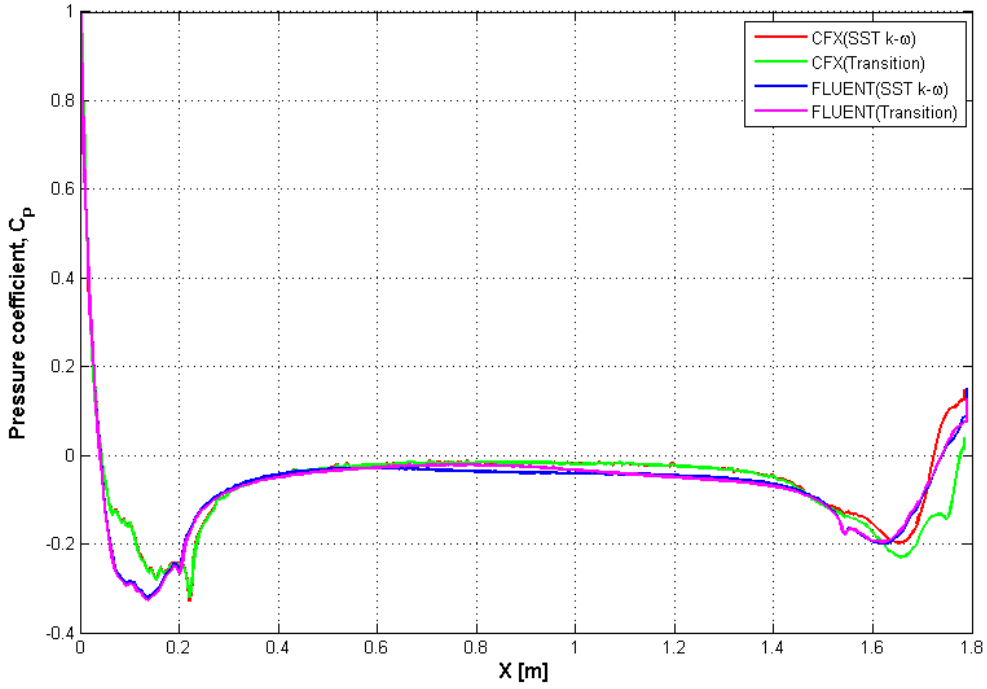

Figure 37. Pressure coefficient along the centerline at 0.3 m/s

The pressure is acting along the local normal direction everywhere along the surface. In order to calculate the effective value contributed to the drag force, the end-view projected area is applied to the pressure. Equation 4 shows the effective pressure coefficient acting in the x-direction. Figure 38 shows the effective pressure coefficient along the centerline.

$$C_{PX} = \frac{P - P_{\infty}}{1/2\rho V_{\infty}^2} \bullet n_x \tag{4}$$

where n_x is the x-component of the normal vector to the surface.

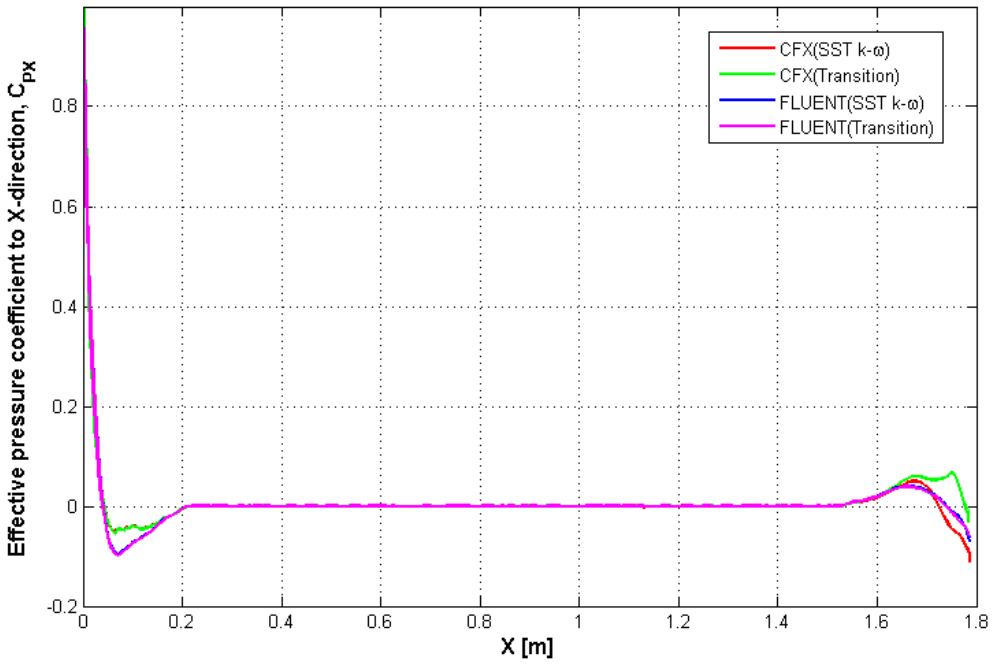

Figure 38. Effective pressure coefficient along the centerline at 0.3 m/s

From Figure 38, the reason why the "Transition" turbulence model with CFX has large pressure drag can be explained by the discrepancy in the green curve in both the nose and tail regions.

Figure 39 shows the pressure coefficient of the approach flow velocity of 0.6 m/s. Figure 40 shows the effective pressure coefficient which is contributing to the drag force; at this flow speed the major discrepancy occurs near the nose.

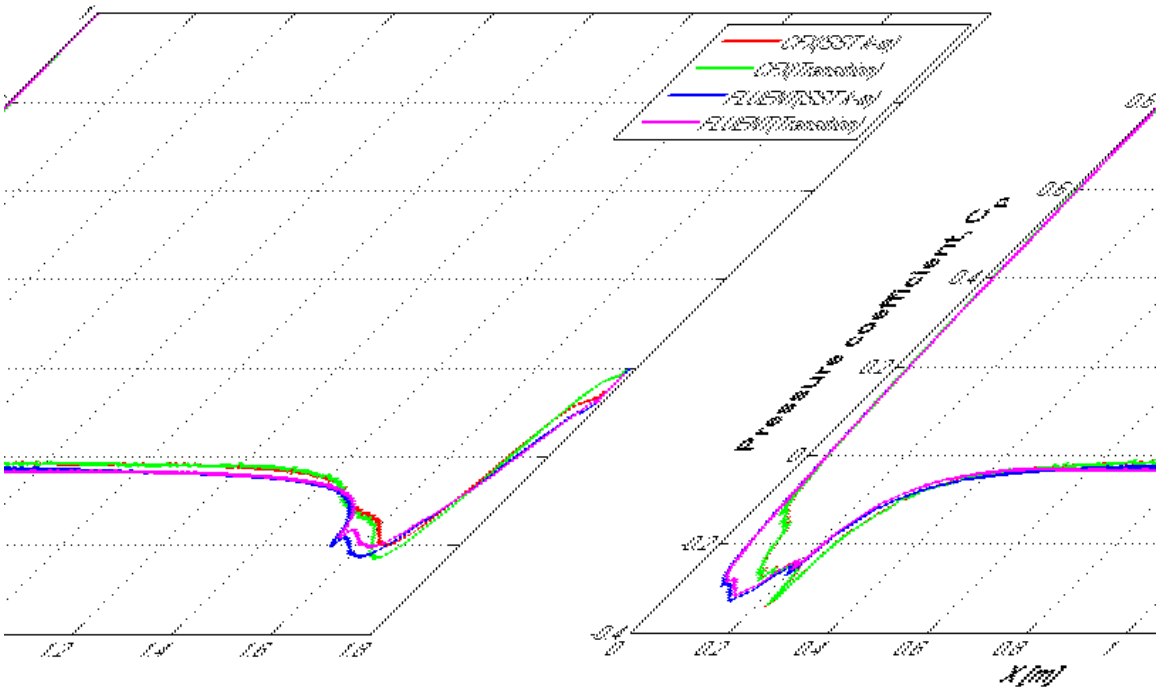

Figure 39. Pressure coefficient along the centerline at 0.6 m/s

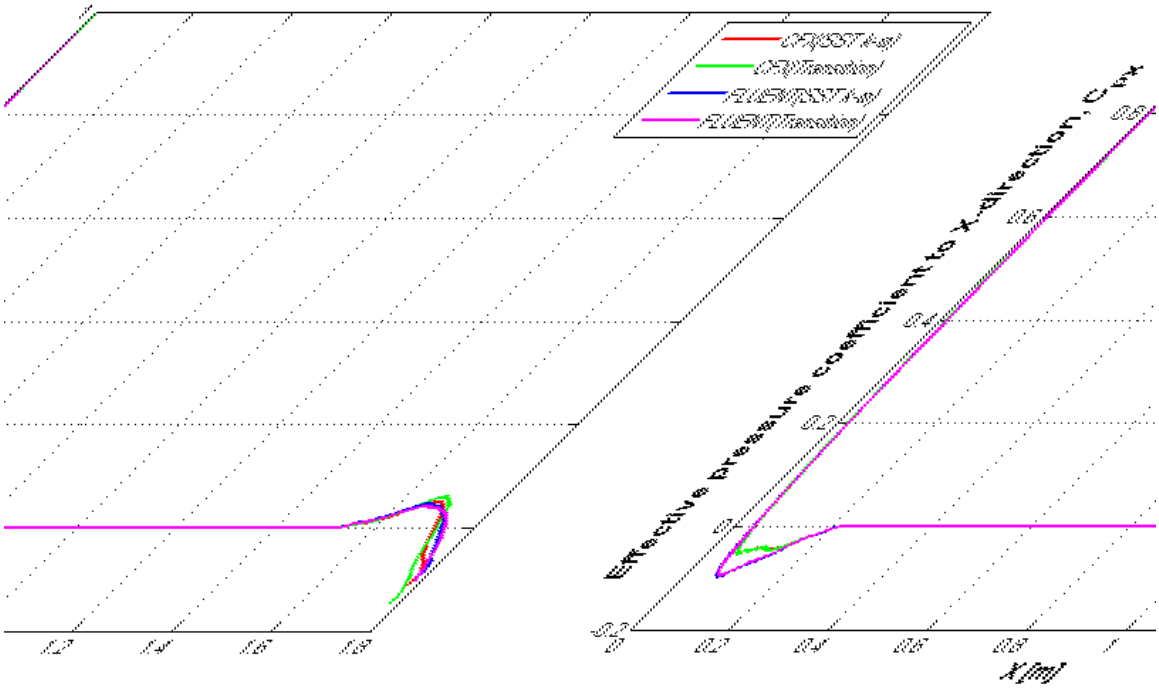

Figure 40. Effective pressure coefficient along the centerline at 0.6 m/s

Figure 41 shows the wall shear stress along the centerline. As shown in this figure, it is apparent that the "Transition" turbulence model of CFX (the green curve) produces the smallest viscous drag of the four cases. In the case of the "Transition" turbulence model with CFX, almost the whole body is immersed in a laminar boundary-layer flow, which corresponds to a small wall shear stress compared with the same body when exposed to a turbulent boundary-layer flow.

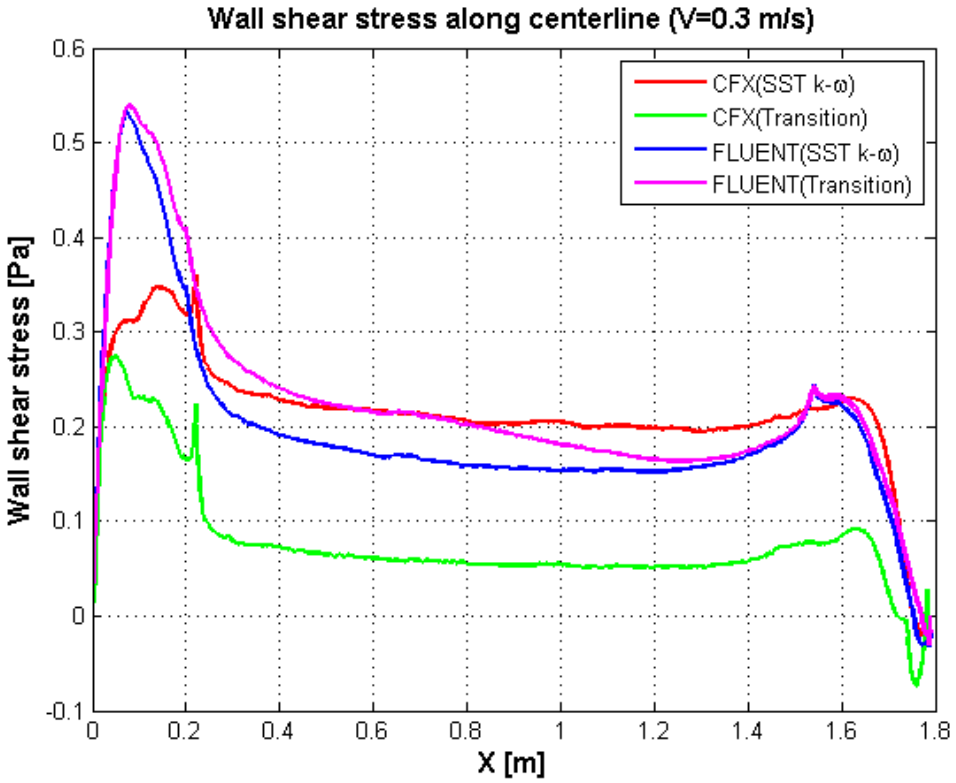

Figure 41. Wall shear stress along the centerline at 0.3 m/s

Figure 42 shows the wall shear stress at the approach flow velocity of 0.6. As shown in this figure, it is apparent what is the contribution to the viscous drag according to each turbulence model and each CFD code. It is noted that the shear stress predicted by the "Transition" turbulence model with CFX (green curve) is rising rapidly around 1.2 m from the nose as shown in Figure 43 for the distribution of TKE; this sudden change can be also explained by the transition from laminar to turbulent flow within the boundary layer, near that location.

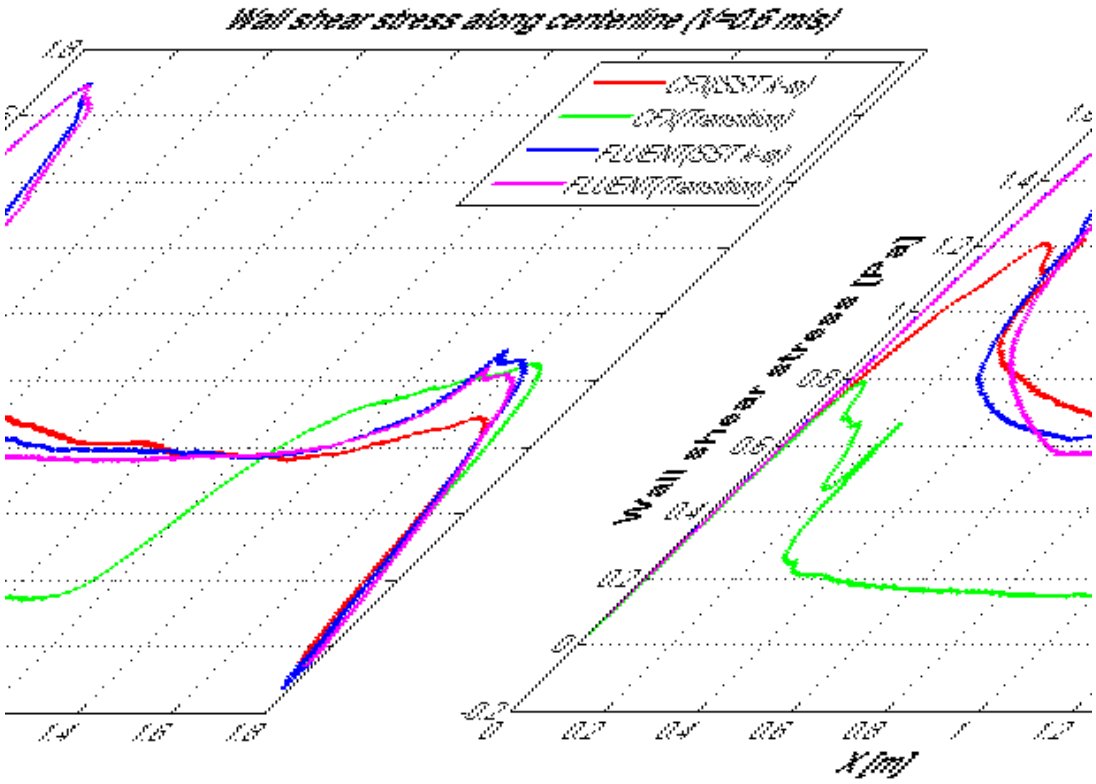

Figure 42. Wall shear stress along the centerline at 0.6 m/s

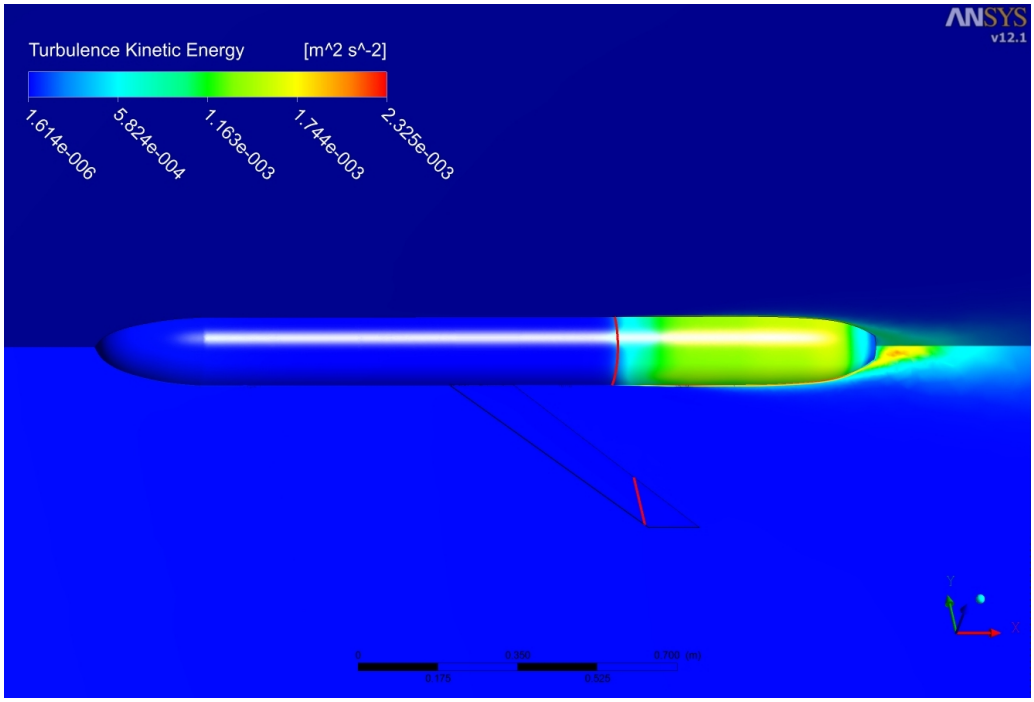

Figure 43. TKE distribution of CFX transition model and red line around 1.2 m (at 0.6 m/s)

The reason why the contribution of the wall shear stress is changed when the approach-flow velocity increases is that the "Transition" turbulence model can change the flow characteristics from laminar to turbulent. As the approach-flow velocity becomes higher, the turbulent region becomes larger. However, in the case of the "Transition" turbulence model of FLUENT, almost the whole body is immersed in a turbulent boundary layer. The difference between the two "SST k-ω" turbulence models of CFX and FLUENT is due to the distribution of normal pressures rather than the distribution of wall shear stress.

4 COMPUTATION TIMES

Table 8 shows typical computation times on a 2.1GHz Pentium® Dual core CPU laptop when using ANSYS CFX version 12.1 and when using ANSYS FLUENT version 12.1 with about 1.8 million elements. The computation time depends on the computing power and the residual level. In this study, it took about 3~6 hours with laptop.

Table 8. Computation times

Velocity (m/s)	CFD Package	SST k-ω model Time (sec)	Transition model Time (sec)
0.3	CFX	6,840	24,340
0.3	FLUENT	13,144	16,744
0.6	CFX	8375	16,470
0.6	FLUENT	15,240	18,239

From the observed computation times and the above results, it appears that either of these CFD packages is suitable and practical for preliminary assessment of the hydrodynamic drag force on a simple axi-symmetric body with wings, when immersed in a flow field at constant angle-of-attack and constant flow speed.

5 CONCLUSIONS

The testing of ANSYS-CFX and ANSYS-FLUENT each with its own version of the "SST k-ω" and "Transition γ-θ" turbulence models produced the following conclusions.

a. Similar visual results were obtained from both CFD packages (with both turbulence models), except in Figures 32 and 36 for the TKE (turbulent kinetic energy).

b. Both CFD packages (both codes with both turbulence models) provide reasonable agreement with the experimental results for the drag force at zero incidence in a constant-speed flow, although the tail-boom, vertical rudder and antenna "dome" for the Slocum ocean glider were not included in this investigation; this suggests that all the CFD predictions for drag force in this report should be lower than the experimental values.

c. On the actual glider and in these computational grids, the wing is represented as a simple flat plate with a blunt leading edge and trailing edge; this may explain the presence of regions of high TKE (turbulent kinetic energy) in the vicinity of the leading edge in Figures 29, 30, 33 and 34.

d. The convergence properties and computational times are reasonable for the type of computer used for these simulations.

e. From the results presented in this report, it appears that either of these CFD packages is suitable and practical for preliminary assessment of the hydrodynamic drag force on a simple axi-symmetric body with wings, when immersed in a flow field at constant angle-of-attack and constant flow speed.

f. The "Transition γ-θ" turbulence model can be applied to the boundary layer flow transition problem, which shows a transition from laminar to turbulent flow as shown in Figures 32 and 36. However, further study concerning the initial conditions such as the initial value for the intermittency parameter is needed.

6 FUTURE WORK

The intention is to add the tail-boom, vertical rudder and antenna dome to the glider mesh and repeat the present investigation using two flow speeds, the same two CFD packages and the same two turbulence models.

The next step will be to perform static runs where the simulations are performed for a range of angles-of-attack (in the pitch plane) and for a range of side-slip angles (in the yaw plane), again for a few constant flow speeds.

Finally the objective is to investigate whether these two CFD packages can represent the flow around, and the hydrodynamic loads exerted on, the glider, while it is performing turning circles while diving or climbing, that is, during helical trajectories while banked; such curved paths will require deflections of the vertical rudder, thus comparisons could be made with full-scale at-sea glider measurements of (i) the diameter of turn, and, (ii) the rate of descent (or ascent), (iii) bank angle etc. probably only for a short segments of the helix due to limitations on the size of the computational domain.

7 LIST OF REFERENCES

[1] ANSYS CFX brochure entitled "Innovative Turbulence Modeling: SST Model in ANSYS® CFX®", available from www.ansys.com/assets/tech-briefs/cfx-sst.pdf

[2] Menter, F.R., "Zonal Two Equation k-ω Turbulence Models for Aerodynamic Flows," AIAA Paper 93-2906, 1993.

[3] Bardina, J.E., Huang, P.G. and Coakley, T.J., "Turbulence Modeling, Validation, Testing and Development," NASA Technical Memorandum 110446, 1997. (See also Bardina, J.E., Huang, P.G. and Coakley, T., "Turbulence Modeling Validation," AIAA Paper 97-2121.)

[4] F.R.Menter et al, "A Correlation-Based Transition Model Using Local Variables - Part I: Model Formulation", Journal of Turbomachinery, Vol. 128, Issue 3, pp. 413 to 423, doi:10.1115/1.2184352, July 2006.

[5] S.M.Salim and S.C.Cheah, "Wall y+ Strategy for Dealing with Wall-Bounded Turbulent Flows", Proc. International Multi-Conference of Engineers and Computer Scientists 2009, vol. II, IMECS 2009, March 2009, Hong Kong.

[6] B.Claus, R.Bachmayer and C.D.Williams, "Development of an Auxiliary Propulsion Module for an Autonomous Underwater Glider", Journal of Engineering for the Maritime Environment, in review, April 2010.

8 LIST OF SYMBOLS, UNIT AND ABBREVIATIONS

Symbol	Description	Units	Page#
C_p	Pressure coefficient	non-dim'l	36
P	Dynamic pressure in the flow	Pa	36
P_∞	Ambient static pressure	Pa	36
ρ	Fluid density	kg/m^3	36
V_∞	Approach-flow velocity	m/s	36
Tu	Turbulence intensity, 100 (2/3 TKE) $^{1/2}$/U	non-dim'l	3
γ	Turbulence intermittency parameter	non-dim'l	3
θ	Boundary layer momentum thickness	m	3
Re_θ	Reynolds Number based on momentum thickness	non-dim'l	3
k	Kinetic energy parameter for turbulent flow	$(m/s)^2$	2
ε	Rate of dissipation of turbulent energy	m^2/s^3	2
ω	Specific dissipation rate of turbulent kinetic energy	s^{-1}	2
y+	Boundary layer parameter for the laminar sub-layer	non-dim'l	5
u*	Friction velocity in the boundary layer	m/s	5
y	Distance to the nearest wall	m	5
ν	Fluid kinematic viscosity	m^2/s	5
u, v, w	Orthogonal components of flow velocity	m/s	27
u(t)	Time-varying component of flow velocity	m/s	27
$\bar{u}$	Mean value of u(t)	m/s	27
u'	Fluctuating component of u(t)	m/s	27
n_x	X-component of the surface normal vector	n/a	37

Abbreviation	Description	Page #
SST	Shear stress transport model	2
CFD	Computational fluid dynamics	1
DSRM	Differential Reynolds Stress Model	5
DES	Detached eddy simulation model	5
LES	Large eddy simulation model	5
SAS	Scale-adaptive simulation model	5
TKE	Turbulent kinetic energy	27